Old Dominion University Research Foundation

DEVELOPMENT OF NUMERICAL MODELS FOR PERFORMANCE PREDICTIONS OF SINGLE-PHOTON AVALANCHE PHOTODECTECTORS (SPAP) FOR THE 2-MICRON REGIME

Final Report for NAG-1-01077

Principal Investigator: Ravindra P. Joshi

DEVELOPMENT OF NUMERICAL MODELS FOR PERFORMANCE PREDICTIONS OF SINGLE-PHOTON AVALANCHE PHOTODECTECTORS (SPAP) FOR THE 2-MICRON REGIME

Final Report for NAG-1-01077

Principal Investigator: Ravindra P. Joshi

DEVELOPMENT OF NUMERICAL MODELS FOR PERFORMANCE PREDICTIONS OF SINGLE-PHOTON AVALANCHE PHOTODETECTORS (SPAP) FOR THE 2-MICRON REGIME

Principal Investigator: Ravindra P. Joshi
Department of Electrical and Computer Engineering
Old Dominion University, Norfolk, VA 23529-0246
(Voice: 757-683-4827 // FAX: 757-683-3220)

NASA Technical Monitor: N. Abedin
Systems Engineering Competency
NASA Langley, Hampton, VA 23681
(Voice: 757-864-4814 // FAX: 757-864-8828)

FINAL REPORT

December, 2001.

Abstract

Field dependent drift velocity results are presented for electron transport in bulk Indium Arsenide (InAs) material based on a Monte Carlo model, which includes an analytical treatment of band-to-band impact ionization. Avalanche multiplication and related excess noise factor (F) are computed as a function of device length and applied voltage. A decrease in F with increases in device length is obtained. The results suggest an inherent utility for InAs-based single-photon avalanche detectors, particularly around the 2 μm region of interest for atmospheric remote sensing applications.

The dark current response was also evaluated. The role of the various components has been analyzed. For shorter devices, the tunneling component is shown to dominate at low temperatures. Finally, possible structures for enhanced photodetection are proposed for future research.

I. INTRODUCTION

Indium Arsenide (InAs) has attracted recent interest for electronic applications because of its small energy gap (about 0.37 eV at room temperature [1,2]) and high electron mobility [3]. InAs is also used as a component for bandgap engineering by growing InGaAs "mixed crystals". The Γ–valley electron effective mass for InAs is only 0.022 m_0 [4-6], but has a relatively high Γ-L valley separation of 1.16 eV. By way of comparison, the effective mass and valley separation values for GaAs are 0.06 m_0 and 0.29 eV, respectively. This implies that the transient transport properties of bulk InAs should be superior, and the velocity overshoot phenomena stronger in this material. This obviously bodes well for fast devices and high frequency electronic applications. In addition, InAs has been proven to be a useful infrared photodetector in the 1–5 μm range [7-11]. Compared to the other narrow-band gap III-V photodetectors, the prime advantage of InAs is that it can operate at room temperature [12], thus avoiding the need for bulky and costly cryogenic cooling systems. This can be a very important consideration in space applications where compactness and low weight are critical. Room temperature operation has prompted the use of InAs in gas hazard detection systems for environmental protection [13,14]. Infrared scintillators based on InAs have also been developed recently [15].

Here, we focus on the high-field transport of InAs and obtain both the transient and steady-state response characteristics. The electronic transport properties of InAs have not been studied previously to the best of our knowledge. Theoretical evaluations of the avalanche multiplication and related excess noise factor are also made. The present study is guided, in part, by a need to ascertain the usefulness of Indium Arsenide (InAs) has attracted recent interest for electronic applications because of its small energy gap (about 0.37 eV at room temperature [1,2]) and high electron mobility [3]. InAs is also used as a component for bandgap engineering by growing InGaAs "mixed crystals". The Γ–valley electron effective mass for InAs is only 0.022 m_0 [4-6], but has a relatively high Γ-L valley separation of 1.16 eV. By way of comparison, the effective mass and valley separation values for GaAs are 0.06 m_0 and 0.29 eV, respectively. This implies that the transient transport properties of bulk InAs should be superior, and the velocity overshoot phenomena stronger in this material. This obviously bodes well for fast devices and high frequency electronic applications. In addition, InAs has been proven to be a useful infrared photodetector in the 1–5 μm range [7-11]. Compared to the other narrow-band gap III-V photodetectors, the prime advantage of InAs is that it can operate at room temperature [12], thus avoiding the need for bulky and costly cryogenic cooling systems. This can be a very important consideration in space applications where compactness and low weight are critical. Room temperature operation has prompted the use of InAs in gas hazard detection systems for environmental protection [13,14]. Infrared scintillators based on InAs have also been developed recently [15].

Here, we focus on the high-field transport of InAs and obtain both the transient and steady-state response characteristics. The electronic transport properties of InAs have not been studied previously to the best of our knowledge. Theoretical evaluations of the avalanche multiplication and related excess noise factor are also made. The present study is guided, in part, by a need to ascertain the usefulness of InAs for single-photon detectors in the Geiger mode at the 2 μm wavelengths that are of interest to space applications. Single-photon avalanche photodetectors [16, 17], appear to be ideal components for high sensitivity detection of the low intensity signals encountered in space. Such electronic devices provide large internal gain yielding strong

current pulses with superior signal-to-noise characteristics. Compared to photomultiplier tubes, the semiconductor based single-photon avalanche photodetectors (SPAP) offer several advantages that include ruggedness, low operating voltage, compact size, low cost, and reliability. These devices are typically reversed biased (Geiger mode) above the breakdown voltage, which helps provide signal amplification (and hence, photon detection efficiency), while maintaining ultrafast response times. Detection efficiencies in the 70 % range with sub-nanosecond timing jitters have been achieved [18]. Better performances in terms of lower dark currents and faster speeds, can be attained by mounting the SPAP devices on two-stage thermoelectric coolers [19]. For successful operation, active quenching can be used, in which electronic circuits monitor the leading edge of every avalanche current and rapidly lower the applied bias [20]. Such active quenching effectively works to reduce the device "dead time", and is imperative when high photon count rates are required. For such SPAP applications, InAs seems promising given the relatively large ratio of its electron to hole effective masses. This disparity should lead to a quenching of the hole-initiated impact ionization, and hence, lower the noise characteristics. In theory, it should also be possible to fabricate separate absorption and multiplication regions similar to the structures that have been used for GaAs [21-23] for achieving detectors characterized by low noise and a high gain-bandwidth product.

Though SPAP devices have been fabricated and used for various applications, microscopic analyses of the device response and electrical characteristics have not been carried out. Furthermore, most of the theory developed is based on quasi-equilibrium treatments for the photogenerated carriers. These approaches can therefore, at best, be applied to relatively long devices with dimensions well beyond the sub-micron range. Similarly, the quasi-equilibrium assumption restricts the predictions to relatively longer times, and makes the results invalid for time scales that are in the sub-nanosecond regime. For example, the excess noise factor "F" is usually obtained from the McIntyre theory [24] in terms of the electron-to-hole ionization coefficient "k" as : $F = k \langle M \rangle + (2 - \langle M \rangle^{-1}) * (1-k)$, where $\langle M \rangle$ is the mean multiplication within the device. However, as shown by Van Vliet et al. [25], the continuous McIntyre theory is no longer applicable when the number of ionizations per primary carrier transit is small, as in short devices. The inaccuracy for small transit distances arises for two reasons: (i) The distances, and hence times, are too short for the carrier (electron or hole) populations to reach quasi-equilibrium. Hence, the "heated Maxwellian" type of distribution functions cannot be used, and are in error. (ii) The "dead space" occupies a larger fraction of the transit distance. Hence, non-local and memory effects become important, and the non-Markovian behavior needs to be included. Application of the continuum theories to experimental data, as done by Hu et al. [26] for example, can lead to unreasonable values of the ionization coefficient ratios. The dead space issues becomes important for the following cases: (i) Injection of primary carriers into short regions of high electric field. Transit distances may then be insufficient for carriers to attain the impact ionization threshold. (ii) Optical generation of primary carriers at random locations within the high field region, (iii) Secondary carrier creation at arbitrary positions, and (iv) Primary carriers that have undergone an impact ionization event and are located arbitrarily within the device. Van Vliet et al. [25], the continuous McIntyre theory is no longer applicable when the number of ionizations per primary carrier transit is small, as in short devices. The inaccuracy for small transit distances arises for two reasons: (i) The distances, and hence times, are too short for the carrier (electron or hole) populations to reach quasi-equilibrium. Hence, the "heated Maxwellian" type of distribution functions cannot be used, and are in error. (ii) The "dead space" occupies a larger fraction of the transit distance. Hence, non-

local and memory effects become important, and the non-Markovian behavior needs to be included. Application of the continuum theories to experimental data, as done by Hu et al. [26] for example, can lead to unreasonable values of the ionization coefficient ratios. The dead space issues becomes important for the following cases: (i) Injection of primary carriers into short regions of high electric field. Transit distances may then be insufficient for carriers to attain the impact ionization threshold. (ii) Optical generation of primary carriers at random locations within the high field region, (iii) Secondary carrier creation at arbitrary positions, and (iv) Primary carriers that have undergone an impact ionization event and are located arbitrarily within the device.

Better models have been developed to account for the dead space and improve the accuracy in predicting detector characteristics. Lukaszek et al. [27] were the first to study this problem. Van Vliet et al. [28] assumed that impact ionization could only occur a finite number of points, each an integral number of dead spaces away from the birth location of the primary carrier. This work demonstrated that the McIntyre theory overestimated the noise factor. A more general scheme was proposed by Marsland et al. [29] which involved the solution of integral equation by a simple recursive technique based on the "lucky drift" model [30]. Saleh et al. developed analytical expressions [31], but their work was restricted to k=0 case and assumed a uniform electric field. The most recent development has been the use of Monte Carlo methods in the calculation of excess noise and carrier multiplication factors for GaAs [32].

II.A MONTE CARLO TRANSPORT SIMULATION DETAILS

Here Monte Carlo (MC) calculations have been carried out to analyze both the transient drift velocity behavior and steady state field dependent characteristics of electrons in bulk InAs. This method takes account of the non-local and distributed effects, the stochastic nature of impact ionization and secondary carrier formation, and temperature variations through the carrier-phonon scattering rates. Details of our kinetic, stochastic MC technique can be found elsewhere [33,34]. Basically, this method treats the carriers as point charges moving within the semiconductor. Motion of the point charges is simulated as a random sequence of free flights governed by Newton's laws, peppered by instantaneous collisions. The frequency of the collisions depends on the collective scattering rates of all the mechanisms. Ensemble averages over the entire population of simulated carriers then yields the transport parameters of interest at each time step. For accuracy, the time step Δt has to be much smaller than the mean time between collisions, in order to capture each scattering discrete event. Here, Δt was taken to be 0.5 femtosecond. A total of 15,000 particles were used for the simulations.

A two-valley model has been used to take account of the Γ- and L-electrons, and two non-degenerate heavy-hole bands used. Most of the material parameters were chosen from the literature [1-2, 4], and the actual values used are given in Table I. For the transport calculations, the L-valley was taken to be parabolic in the absence of any direct data, while the Γ–valley was treated in terms of a simple non-parabolicity factor $\alpha = 2.4$ eV^{-1}. However, non-parabolicity was ignored for the high-field calculations of the multiplication factor. The

Monte Carlo treatment of hole scattering was based on a model for hole transport in polar materials described in detail by Costato et al. [35]. It included hole interactions with acoustic modes via the deformation potential mechanism, polar optical phonon processes, and non-polar optical scattering. Unlike most numerical treatments, the acoustic phonon scattering was treated here as an inelastic process. For acoustic interactions, it is typically assumed that the thermal energy is much lower than the phonon quanta (i.e. $k_B T << \hbar\omega$). This then leads to an assumption of elastic scattering and use is made of the equi-partition approximation to simplify the phonon occupancy term. Though generally valid at room temperature, the more rigorous model was implemented here. Polar-optical scattering is important, and its important to hole transport was first pointed out by Kranzer [36]. Screening of the polar interactions was evaluated within the random phase, zero-frequency approximation [37]. For the transport calculations (given in the next section) a fixed density of 10^{16} cm^{-3} was used. Also, both the interband and intraband scattering events were taken into consideration. Interband scattering for electrons was treated using a single effective deformation potential, assumed to take account of the various symmetry-allowed phonon processes. Finally, impurity scattering was ignored in this treatment for the following reasons. First, neglecting impurity scattering would naturally yield a theoretical upper limit on the transport characteristics. Next, since the present aim is to ascertain the suitability of bulk InAs material for high-speed photodetectors, there would be no intentional impurities present under these conditions. Such devices would employ near-intrinsic material to lower noise, and decrease impurity scattering related speed reductions.

As first shown by Lax and Mavroides [38] based on the methods developed by Kane [39], valance bandstructure for III-V compounds is best represented through a nonquadratic relation between the carrier kinetic energy E(k) and the wavevector "k". Dresselhaus [40] showed that the valance band energy has the form:

$$E(k) = E_v \pm C\{k^2 \pm [\,3\,(k_x^2 k_y^2 + k_x^2 k_z^2 + k_z^2 k_y^2)\,]^{0.5}\}^{0.5} \quad , \qquad (1)$$

where E_v is the valance band value at $k \equiv 0$, and C is a material dependent constant. Due to the presence of linear k-terms, each of the heavy and light-hole bands are split into two non-degenerate bands and the energy maxima shifted from the $k \equiv 0$ point. As shown by Roberts et al. [41], the energy maxima are located on the <111> and <100> axes with the isoenergetic surfaces being ellipsoids of revolution. Based on this formulation, the shift in the energy extremum ΔE_m is given as: $\Delta E_m = (m_v C^2 / \hbar^2)$, with m_v being the effective hole mass. The results of Matossi and Stern for InAs [42] yield: $m_v = 0.41\ m_o$, and $\Delta E_m = 6$ meV where $m_o = 9.1 \times 10^{-31}$ Kg is the electronic rest mass.

In order to study the physics of single photon avalanche detectors, it becomes necessary to accurately include the impact ionization (I.I.) process. Hence, this aspect is discussed next. Early theories assumed that carriers could attain the II threshold either by avoiding collisions during drift [43], or undergoing many collisions while continually gaining energy [44]. While Baraff [45] combined the two theories, the formulation failed to predict the I.I. rate without resorting to adjustable parameters. More extensive numerically based treatments have emerged [46-49], and include a progression from simple parabolic bands to the inclusion of full bandstructures [50-52]. However, some of the more sophisticated approaches are computationally very

intensive, and often the I.I. rate is calculated via the well-known but simple Keldysh formula [53]. Here, we have attempted to use a relatively simple semi-classical approach without a full bandstructure calculation, but does go beyond the Keldysh formula. The more subtle transport issues such as the intra-collisional field effect and energy-time uncertainty [54] have been excluded.

The analytical treatment of I.I. presented by Quade et al. [55] is followed here. Fig. 1 shows the general energy-band diagram relevant to the I.I. process. An electron initially in state $\mathbf{k}_1$ and band α makes a transition to state $\mathbf{k}_1'$ in band β, while the other participating electron in state $\mathbf{k}_2$ and band δ shifts to state $\mathbf{k}_2'$ in band γ. The I.I. rate G is given in this picture by [56]:

$$G = \Sigma_{k1,\,k1',\,k2,\,k2'} P_{ii}(\mathbf{k}_1,\mathbf{k}_1',\mathbf{k}_2,\mathbf{k}_2') [1-f(\mathbf{k}_1)] f(\mathbf{k}_2) [1-f(\mathbf{k}_1')] [1-f(\mathbf{k}_2')] \ , \quad (2)$$

where $f(\mathbf{k}_i)$ are the nonequilibrium carrier distribution functions. For non-degenerate statistics (as encountered in a single photon photodetector), the rate simplifies to:

$$G = \Sigma_{k2} P_{ii}(\mathbf{k}_2) f(\mathbf{k}_2) \ . \quad (3)$$

A simple direct band transition for InAs will involve an initial pair of electrons, one in the heavy-hole band and the other in the Γ-valley, with final states in the Γ-valley. For this situation, one would set: $m_\alpha = m_v$; $m_\beta = m_\delta = m_\gamma = m_c$; $\mathbf{Z}_\alpha = \mathbf{Z}_\beta = \mathbf{Z}_\gamma = 0$; $\varepsilon_\beta = \varepsilon_\gamma = 0$; $\varepsilon_\alpha = [2\, m_c E_{gap}/\hbar^2]$; $E_\delta = [\hbar^2 k^2/(2m_c)]$, with E_{gap} being the direct energy gap, $m_{v,c}$ the valence and Γ-valley masses. The scattering rate $P_{ii}(k)$ for $\mathbf{Z}_\alpha \neq 0$ is given to be [55] :

$$P_{ii}(k) = (0.5/\tau) [\{(k^2+Z^2 -2\mathbf{Z}.\mathbf{k})/(k_{th}^2 +Z^2 +2Zk_{th})\}^{0.5} + \{(k_{th}^2 +Z^2 +2Zk_{th})/(k^2 +Z^2 -2\mathbf{Z}.\mathbf{k})\}^{0.5} -1] \ , \quad (4)$$

where $\mathbf{Z} = [\alpha/(1+\alpha)]\, \mathbf{Z}_\alpha$; $\alpha = m_c/m_v$; $\tau = [\pi^2 \varepsilon^2 \hbar^3 (1+\alpha)^{1.5}]/[e^4 m_c \mu^{0.5}]$; $\mu = (1+2\alpha)/(1+\alpha)$, with ε the InAs permittivity, and $k_{th} = \{[\mu\{\varepsilon_\alpha + (1+1/\alpha)\, Z^2\}]^{0.5} - Z\}$ being the threshold wavevector. With $\mathbf{Z}_\alpha = 0$, the threshold wavevector simplifies to the following standard expression :

$$k_{th} = \{[(1+2\alpha)/(1+\alpha)]\, [2\, m_c E_{gap}/\hbar^2]\}^{0.5} \ , \quad (5a)$$

$$\text{and,} \quad P_{ii}(k) = (0.5/\tau)\, [k/k_{th} + k_{th}/k - 1] \ . \quad (5b)$$

In general, the threshold energies for impact ionization and the I.I. rates can be computed for all of the relevant transition for InAs following the procedure outlined by Quade et al. [55]. The threshold wavevetor k_{th} is obtained as the solution of the following general equation:

$$k_{th}\nu^2 + k_{th}\, [2\, \nu\mu Z_\gamma - 2\nu^2 Z_\gamma - 2\nu(Z_\alpha - Z_\beta)\{\alpha\beta/(\alpha+\beta)\}] + \{[(Z_\alpha - Z_\beta)\{\alpha\beta/(\alpha+\beta)\}]^2 +$$
$$+ \nu^2 Z_\gamma^2 + 2\nu\, Z_\gamma\, (Z_\alpha - Z_\beta)\alpha\beta/(\alpha+\beta) - \mu[\varepsilon_0 + \{\alpha\beta/(\alpha+\beta)\}(Z_\alpha - Z_\beta)^2\} = 0 \ , \quad (6a)$$

where,

$$\mu = (\alpha\beta + \alpha\nu + \beta\nu)/(\alpha+\beta) \ , \quad (6b)$$

$$\alpha = m_\delta/m_\alpha\ ,\ \beta = m_\delta/m_\beta\ ,\ \nu = m_\delta/m_\gamma\ ,\quad (6c)$$

$$\text{and,}\quad \varepsilon_0 = \varepsilon_\beta + \varepsilon_\gamma + \varepsilon_\alpha\ .\quad (6d)$$

In this contribution the following six I.I. processes were considered: (i) {Γ, HH → Γ,Γ} , (ii) {Γ, HH → Γ, L}, (iii) {Γ, HH → L,L} , (iv) {L, HH → L, L} , (v) {L,HH → Γ,L} , (vi) {L, HH → Γ, Γ}. Here hole initiated events were ignored for simplicity. In our Monte Carlo simulation scheme, the selection of final states after impact ionization was carried out based on a random assignment of the states $\mathbf{k}_1'$ and $\mathbf{k}_2'$. This procedure has been used in the past, and guarantees that both electrons are not distinguishable after scattering [51]. The state of the valance band quasi-particle was then calculated based on energy and momentum conservation. If this did not result in a real k-space state, then the random selections were rejected and another assignment made.

II.B DARK CURRENT CALCULATIONS

Dark currents in a reverse biased junction avalanche photodiode(both p-n and p-i-n structures) are can be easily calculated by taking account of the three following processes: (a) Diffusion currents, (b) Bulk generation currents, and (c) Tunneling currents. Of these, the tunneling component is usually quite small and mainly arises from the Zener process. Expressions for all three conduction mechanisms are well known, and are given below for completeness. Calculations were performed to gauge the dark-current characteristics based on the mathematical expressions presented here.

(i) Diffusion current $J_{Diff.}$: Under strong reverse bias conditions, the expression for the diffusion current is

$$J_{Diff.} = q\, n_i^2\, \{[D_n/\tau_n]^{0.5}\}/N_A + \{[D_p/\tau_p]^{0.5}/N_D\}\ ,\quad (7a)$$

where $D_{n,p}$ are the electron and hoe diffusion coefficients, $N_{A,D}$ the acceptor and donor doping densities, $\tau_{n,p}$ the minority carrier lifetimes of electrons and holes, and n_i the intrinsic carrier concentration. As well known, n_i depends on the temperature T, the bandgap E_g and the electron/hole effective masses $m_{e,h}$ and is given as:

$$n_i = 2\,[k_B^2\, m_e\, m_h/\{4\pi^2\, \hbar^4\}]^{0.75}\, T^{1.5}\, \exp[-E_g/(2k_BT)]\ .\quad (7b)$$

(ii) Bulk generation current $J_{Gen.}$: The generation current under conditions of reverse bias is given by:

$$J_{Gen.} = q\, n_i\, W/\tau_{eff}\ ,\quad (7c)$$

where W is the width of the transit/depletion region, and τ_{eff} the effective carrier lifetime.

(iii) Tunneling/Zener current $J_{Tun.}$: The tunneling/Zener current is generally small. Unlike, indirect bandgap materials, though, its contribution in direct bandgap semiconductors is not totally negligible. This current as a function of the reverse bias V is given by the following expression [57] with $V_p \sim 0.2$:

$$J_{Tun.} = q^3 V^2 /(18\,\pi W\,\hbar^2)\,[m_e / E_g]^{0.5} \exp[1+V/V_p] \exp[-(\pi W\,\{m_e E_g^{\,3}\}^{0.5}) / (2^{1..5} q\,\hbar V)] \quad . \qquad (7d)$$

IIIA. TRANSPORT RESULTS AND DISCUSSION

Results of the transient electron drift velocities obtained from Monte Carlo simulations at 300 K are shown in Figs. 2 for applied electric fields of 1, 4 and 8 kV/cm. The raw data obtained was not absolutely smooth, but had very small fluctuations. Statistically, the fluctuations are expected to scale as $1/N^{0.5}$ with N being the total number of particles simulated. Due to the large population of the ensemble, the variations were quite small. Here the data points were deliberately smoothened, and so the small deviations are not seen. At the lowest field of 1 kV/cm, the drift velocity increases monotonically with time, and then saturates to a value of about 3×10^5 ms^{-1}. The occurrence of a velocity overshoot is evident from the plots for the 4 kV/cm and 8 kV/cm fields. The overshoot arises from inter-valley electron transfer, as originally explained in the context of GaAs [58,59]. The transfer characteristics into the L-valleys from the Γ–valley for a few field values are shown in Fig. 3. The six curves represent the temporal variation of the electron populations for the step electric field inputs of 0.5 kV/cm, 4 kV/cm and 8 kV/cm. Clearly, at the lowest field of 0.5 kV/cm, almost all of the electrons reside in the Γ–valley. This percentage decreases to about 58 % at the 8 kV/cm value. Even at this highest 8 kV/cm field, there is a delay of about 0.6 picoseconds, after which the L-valley populations begin to increase. This delay simply reflects the time required for the Γ–valley electrons to gain sufficient energy from the external field to begin transcending the inter-valley threshold. Next, the electron velocity-field characteristics were obtained from the transient curves by letting the Monte Carlo simulations run until a clear steady state was achieved. The results are shown in Fig. 4. A relatively sharp overshoot is clearly evident, and represents the highest drift velocity attainable under stationary conditions. This value is about 3.8×10^5 ms^{-1}, and occurs at an external electric field slightly beyond 2 kV/cm. These characteristics compare well with a recent report by Hori et al. [60]. The slope from Fig. 4 at low electric fields, yields a mobility of about 1.45 m^2 $V^{-1}s^{-1}$. This is in the range measured by Souw et al. [61] for their low defect samples grown at higher temperatures.

It is interesting and useful to compare these results with the transport data for GaAs, a material that is currently in common use for electronic devices. The GaAs steady-state velocity peak at 300 K in the absence of impurity scattering is about 2×10^5 ms^{-1} [62]. In this regard, bulk InAs is predicted to be about twice as fast. This arises from an InAs Γ–valley electron mass of 0.022 m_o that is about three times smaller compared to the 0.06 m_o value for GaAs. The ratio of the peak steady-state velocities between the two materials is less than a factor of three because of the heavier L-valley InAs electron mass. The threshold electric field corresponding to this peak velocity is about 50 percent smaller than the 4kV/cm value for GaAs. This is again associated with the smaller effective mass, which enables InAs electrons to gain more kinetic energy. Again, the electric fields are not in proportion to the effective masses because of the slightly higher intervalley separation for InAs. Furthermore, with a saturation velocity of about 1.65×10^5 ms^{-1} (as compared to ~0.8×10^5 ms^{-1} for GaAs), the high-field characteristics are also much better. The transient characteristics for InaAs are vastly superior to GaAs as well. For example, the transient peak at 8 kV/cm from Fig. 2 is about 1.7×10^6 ms^{-1} , while the

corresponding magnitude for GaAs is only about 3.5×10^5 ms^{-1} [63]. This bodes well for transient transport based high cut-off frequency response, sensitive photodetection and rapid photon counting. For InAs, the following factors collectively contribute to superior transport characteristics. The lower density of states and effective mass influence the transition rates and tend to reduce scattering. The lower acoustic deformation potential also has a similar result of reducing acoustic phonon scattering. Finally, the smaller optical phonon energy quanta $\hbar\omega$ reduces phonon energy emissions, and leads to increased kinetic energy.

It is perhaps useful for device modeling applications to obtain a closed form analytical expression for the velocity-field characteristic. The velocity $v_n(E)$ for GaAs can roughly be fit by the following curve [64] :

$$v_n(E) = [\mu_n E + v_{sat} (E/E_p)^{\beta}] / [1 + (E/E_p)^{\beta}] \quad , \quad (7)$$

where μ_n is the low field mobility, E the applied electric field, E_p the field corresponding to the peak steady-state velocity, β an adjustable parameter, and v_{sat} the saturation drift velocity. The values for GaAs are: $E_p = 4$ kV/cm, $\mu_n = 0.62$ $m^2V^{-1}s^{-1}$, $v_{sat} = 0.8 \times 10^5$ ms^{-1} , and $\beta = 4$. Using the same analytical form for InAs, the parameters can be obtained from a best fit to the velocity-field curve of Fig. 4. For InAs, the effective saturation velocity v_{sat} works out to be about 1.65×10^5 ms^{-1}, a mobility parameter μ_n of 2.9 $m^2 V^{-1} s^{-1}$, $\beta = 4$, and $E_p = 2$ kV/cm. This best fit mobility value compares very well with published experimental data [65], thus providing an indirect validity check of the present MC results.

After obtaining reasonable agreement with published InAs transport data, the MC code was applied to study the high-field behavior, particularly the impact ionization process and field-dependent multiplication characteristics. The principle aim was to assess the performance of possible InAs based single photon, p-i-n detectors at 2 μm for space applications. In keeping with this objective, the MC scheme was used to simulate the photo-generation, subsequent transport and avalanche multiplication of single electron-hole pairs randomly generated within the intrinsic region, with a 2 μm total pair-energy. Thus, unlike traditional MC implementations for impact ionization studies wherein electrons are always injected at one boundary, or a specific contact, or one end of a space-charge region, the carriers here were assigned a random starting spatial distribution. Due to this stochastic initial position, it is expected that the multiplication factors derived from the present simulations would be less than those for avalanche devices that rely on electrical injection. The transitions were assumed to take place between the Γ–valley and both the two heavy-hole and light-hole bands, in proportion to their respective joint density-of-states. The width of the p-i-n structure was a specified input parameter of the simulation, and the depletion approximation used to compute the internal electric field for a given external bias. The motion of the primary carriers was followed, and all secondary carriers tracked until the ultimate emergence of every particle (primary and off-spring) from the simulated device region. The multiplication factor, M, was thus computed by recording the total number of particles produced starting from each electron-hole pair. For statistical accuracy, an average value $\langle M \rangle$ was obtained by repeating the simulation at each applied voltage and device length, for many different random seed values. Besides, $\langle M \rangle$, this MC simulation also allows a determination of $\langle M^2 \rangle$ and the excess noise factor F evaluated as [32] : $F = \langle M^2 \rangle / \langle M \rangle^2$.

Results for the average multiplication factor, <M>, as a function of the electric field for different device simulation lengths are shown in Fig. 5. As might be expected, the breakdown threshold field, which corresponds to the sharp vertical increases in the curves, is higher for smaller device lengths. This in itself is a direct consequence of the "dead space" inherent to the impact ionization process. Conventional theory would not provide for such an electric field dependence on the device size. The dead-space effects is more critical in this context of photo-generation, since the initial creation occurs randomly within the entire length, and some carriers can, in principle, be generated very close to the collecting electrode. Conversely, at a given electric field, the net multiplication is predicted to be much larger for a longer intrinsic region. The threshold electric field, from Fig. 5, is seen to roughly scale down with increasing device length. As a result, the total avalanche voltages for devices of varying lengths (at least for the 0.4 – 10 μm range shown), are all roughly comparable. This can be understood in terms of a total energy gain requirement for carrier multiplication, rather than a dependence on the local electric field magnitudes. The variability in M associated with the stochastic fluctuations in the energy and spatial location of the initial photo-generated electron-hole pair is brought out in Fig. 6. A histogram of M is shown in Fig. 6 with the multiplication factor appearing on the x-axis and the number of events corresponding to the M value plotted along the y-axis. For concreteness, a 2 μm device width is shown with an electric field of 50 kV/cm. The distribution in Fig. 6 is quite asymmetric, and displays a statistical mode of unity and a maximum multiplication factor of 45.

Next, based on the MC results for carrier multiplication, the excess noise factor F was computed as a function of the multiplication M for various lengths. The results are shown in Fig. 7. According to McIntyre theory, the excess noise factor F is given in terms of "k", the ratio of electron-to-hole impact ionization coefficients, as: $F = k\langle M\rangle + (2-\langle M\rangle^{-1})(1-k)$. Thus, F is a monotonically increasing function of "k". The "k" value reduces and tends to unity as the electron and hole impact ionization coefficients approach each other. Physically, this can occur as device dimensions increase, since differences in the initial threshold energy and the dead space characteristics between electron- and hole-initiated processes will then gradually disappear. Besides a reduction in excess noise with increasing device length, one can expect a slower differential as dimensions progressively increase due to the asymptotic limit of unity for "k". In a local, continuum approach, the "k" value depends only on the local electric field. Consequently, decreases in the excess noise factor are predicted with increasing electric field, as k approaches unity. However, due to the non-local nature of impact ionization, the finite dead-space characteristics, and the possibility of only finite number of collisions in a small device, the argument of a decrease in F with increasing field does not necessarily hold.

Here, MC simulations were used to evaluate the excess noise factor in terms of the average and mean-square multiplication as : $F = \langle M^2\rangle/\langle M\rangle^2$. The curves of Fig. 7 show the results of the InAs photo-detector noise characteristics for device lengths ranging from 0.04 μm, 0.4μm, and 10.0 μms. The following features are evident. (i) The F value is highest for the smallest 0.04 μm device. This is in keeping with the reasons given above. (ii) The differential change in F with dimension reduces in going from 0.04 μm through 0.4 μm and then 10.0 μm, again in keeping with expectations. Thus, there are no significant advantages in terms of the excess noise, in continuing to make the devices longer. (iii) For a given value of <M>, the value of F is highest in the smallest device due to the higher statistical variance associated with the dead-space. The initial random location of the particles created through the photo-generation process adds to this variance. (iv) Finally, the

excess noise increases monotonically with <M> for any given device length. Higher fields lead to larger <M> values, but this comes at the expense of higher scattering which tends to increase fluctuations within the system.

IIIB. DARK CURRENT RESULTS AND DISCUSSIONS

Results of the dark current in InAs p-i-n photodetectors are given and discussed next. In order to ascertain the validity of the predicted results, dark current simulations were carried out for specific devices whose characteristics have been reported in the literature. The aim was to facilitate direct comparisons between predictions of the present theoretical model and experimentally measured data. Towards this end, the bulk InAs p-i-n devices of Kuan et al. [66] were chosen. The geometric size (for example, circular area with a 150 μm diameter), doping, ambient temperature and applied bias were then taken to correspond to their reported devices.

Simulation result of the dark current for a device width of 0.14 μm and doping densities $N_A = 3 \times 10^{17}$ /cc, $N_D = 5 \times 10^{16}$ /cc at a reverse bias of 1.0 V are shown in Fig. 8 as a function of inverse temperature. The electron and hole lifetimes were taken to be 10 ns, the electron and hole effective masses were assigned values of $0.0235m_o$ and $0.4\ m_o$, respectively, while the electron and hole mobilities were $0.2\ m^2\ V^{-1}\ s^{-1}$ and $1.45\ V^{-1}\ s^{-1}$, respectively. Shown in Fig. 8 are the diffusion, generation, tunneling, and total currents. The value of tunneling component was relatively negligible above temperatures of 340 Kelvin. However, at room temperature and below, the tunneling current is seen to dominate. Since this current is insensitive to the temperature, while both the diffusion and generation components reduce exponentially with decreasing temperature, the current flattens out to a near constant value at low temperatures. The total current at room temperature is predicted to be about 7×10^{-4} Ampere, a value that agrees very well with the experimental data of Kuan et al. [Fig. 1, Ref. 66]. Also, the near constant current below 250 Kelvin match the Kuan results. This close comparison lends credibility to the present simulations. With increasing reverse bias, the tunneling currents are expected to increase. This aspect is quantified in Fig. 9, which shows the various current contributions as a function of the applied reverse bias. At a biasing levels of about 0.95 Volt and beyond, the tunneling component is predicted to dominate the dark current characteristics of this 0.14 μm device. This roughly corresponds to an internal electric field of 70 kV/cm . Since this field is well below the avalanche breakdown field of Fig. 5, one can expect significant Zener tunneling related dark currents to exist in InAs avalanche photodetectors biased close to their breakdown voltage. One can, in principle, curtail the dark currents dramatically (in an exponential manner), by reducing the applied reverse bias below the avalanche breakdown threshold, while still benefiting from a fairly large avalanche multiplication factor.

Finally, the effect of increasing the device width is shown in Figs. 10a and 10b by focusing on a larger 1.0 μm device. The dependence of current on inverse temperature, shown in Fig. 10a, reveals near suppression of the tunneling component. The generation component is seen to scale up as compared to the corresponding curve of Fig. 8. This is expected based on an increase in the larger depletion width. The curves of Fig. 10b, showing the behavior of the 1.0 μm device at 300 Kelvin as a function of applied reverse bias. Here, the tunneling current is seen to be negligible until voltages of 3.95 Volts, corresponding to fields of 40 kV/cm. It

thus becomes apparent that increases in device width will work to suppress tunneling currents. However, the voltages at which the tunneling components begin to dominate will not scale linearly with width. The trend towards decreased electric fields with device length for tunneling to dominate the dark current, is similar to the reductions in avalanche breakdown fields observed in Fig. 5 for longer devices. It should, therefore, be possible to bias longer devices at voltages that are not scaled linearly, without bringing down the multiplication factor significantly. Finally, it seems advantageous to operate longer p-i-n avalanche photodiodes at low temperatures to suppress the dark currents.

IIIC. IMPULSE RESPONSE RESULTS AND DISCUSSIONS

The impulse response is an important parameter that characterizes the response speed, frequency response, and provides the transfer function for the device. In the context of a single-photon avalanche photodetector, the impulse response amounts to the temporal behavior of photocurrent generated by a short optical pulse producing limited electron-hole pairs. Such an impulse response can be ascertained most conveniently by carrying out Monte Carlo (MC) drift simulations of the initially generated electron-hole swarm for a given device geometry, applied bias and operating temperature.

In this study, such MC simulations were carried out for carrier generation by a 2 μm optical pulse. The operating temperature was taken to be 300 Kelvin, and 1000 particles were used. Based on a 33 % conversion efficiency, this translated into an input photon energy of 1.976 μJm^{-2}. Fig. 11a shows the temporal evolution of the carrier population for a 1 μm reverse-biased p-i-n device at electric field of 10 kV/cm and 50 kV/cm within the intrinsic region. For both cases, the holes are seen to take a much longer time to be entirely flushed out of the system. This is expected given that the hole drift velocities are much smaller than the values for electrons. The electron and hole curves for 50 kV/cm both show an increase from the initial population of 1000 as secondary carriers are created due to impact ionization. The maximum electron population approaches about 1450 (i.e. a 45 % increase), while the holes exhibit a much stronger 200 % increase. The lower enhancement for electrons is the result of faster flush-out. Furthermore, it becomes apparent from Fig. 11a that electrons take only about 1.0 ps before being completely removed, while the holes remain in the system for as long as 30 ps. At the lower field of 10 kV/cm, on the other hand, the impact ionization is much lower. The electron population always remains below the 1000 level in spite of weak secondary carrier generation. The hole population curve does exceed the 1000 point at around 0.4 ps, and then decreases monotonically beyond 0.6 ps. In this case as well, the time taken for electron removal is relatively short (~ 1.5 ps) as compared to the 30 picoseconds for the holes. The corresponding distribution of electrons amongst the Γ- and L-valleys is shown in Fig. 11b. The curves show that the L-valley populations at both electric fields remain negligible. This is a consequence of initial photogeneration in the Γ-valley, and the high rate of ionization rate of the: $\Gamma \rightarrow \Gamma + \Gamma$ process. Fig. 11c shows the photocurrent response at the two electric fields. The 50 kV/cm curve shows a slight structure below 0.5 ps arising from the collective contributions of the electron and hole current components. Due to the flush out of carriers, and the faster moving holes in particular, the photocurrent is seen to reduce to negligible levels within about 1.5 ps. However, the long "tail" of the hole population causes non-zero current contributions over a prolonged period of time. Also, due to the internal scattering for an ever decreasing population of remaining holes, the photocurrent response is predicted to become fairly noisy beyond

1.5 ps. The peak values for the 10 kV/cm and 50 kV/cm are about 0.22 mA and 0.44 mA, respectively. Thus, the current is not seen to scale with electric field, and is the result of several factors. First, the velocity does not scale linearly with field at high magnitudes. Second, the impact ionization rates also do not vary in proportion to the field, but instead have a strongly non-linear relation even above threshold. Finally, due to higher carrier rates of loss at the higher fields due to larger transient velocities, the current cannot increase as much.

Next, comparisons of the impulse response between devices of differing widths were carried out. The results shown in Fig. 12 were for 1.0 μm and 3.5 μm reverse-biased p-i-n avalanche devices. The predicted temporal behavior for the carrier populations is shown in Fig. 12a for a 10 kV/cm field. The enhancement in density for the 3.5 μm device is predicted to be very strong. Starting from an initial population of 1000 electrons and holes each, the holes reach a maximum count of 5320. The electrons, as before, grow at a much lower rate due to their higher exit rates, and a peak of only 2200 is seen. The electrons in the longer device are predicted to take about 5 ps for complete egress, as compared to the 1.5 ps at the shorter 1.0 μm length. Not surprisingly, these exit times thus roughly scale with distance, given the constant field for both cases. As shown separately in Fig. 12b, the total time necessary for the holes to completely exit the 3.5 μm structure was about 180 ps. The corresponding photocurrents for the 1 and 3.5 micron cases at 10 kV/cm are shown in Fig. 12c. The longer device has a higher peak as expected, and its response is also much faster. While noise is present beyond 1.5 ps, the current has nonetheless fallen to near insignificant levels. The 3.5 μm device, however, is predicted to have non-negligible photocurrents up to about 4.0 ps, with more noise over longer periods.

IV. PROPOSED STRUCTURES FOR ENHANCED PERFORMANCE

(a) A Novel Interdigitated Low-Noise p-n Junction Detector:

The excess noise of an avalanche photodetector strongly depends on the ratio κ of electron-to-hole ionization rates. The noise factor can be minimized if κ is very different from one and the ionization is initiated by the carrier of the highest ionization coefficient. At the long wavelengths (i.e $\lambda \leq 1.06$ μm), most III-V semiconductor materials have $\kappa \rightarrow 1$. The ionization rates can be made to differ significantly if heterojunctions are used, which can then give rise to "real-space transfer" [67]. For example, as shown by Capasso [68], the κ ratio in $Al_{0.45}Ga_{0.55}As$-GaAs superlattices, the ratio can be enhanced ten times by making use of the difference in the discontinuities of the conduction- and valence-band edges. Typically, the conduction band discontinuity ΔE_c is more than twice as large as the valence-band discontinuity ΔE_v. Consequently, electron entering the lower bandgap semiconductor can attain an appreciable increase in their kinetic energy, while holes do not. The result is preferential enhancement of electron-initiated impact ionization, leading to higher κ values, and a quenching of excess noise.

Based on the above difference in ionization between electrons and holes in heterojunctions, and the possibility of tailoring the properties, a new APD structure is proposed in Fig. 13. It is predicted to produce lower noise. In the schematic of Fig. 13, the p-layers have a wider bandgap than the n-layers, and an interdigitated scheme has been shown. The voltage supplying the reverse bias is connected between the p^+ and

n^+ end regions. Fig. 13 assumed equal doping levels for the n- and p-layers, with the three middle layers having thickness "d", while the top and bottom layers are shown to have a thickness d/2 . The layer length L is much larger (i.e. L >> d). In this context, the n- and p-layers could be InAs and InGaAs, respectively. Also, shown is the cross-section of the low-noise, interdigitated p-n junction structure. The shaded portions represent the depletion regions of the device. In Fig. 14a, the white areas represent undepleted portions of the n- and p-regions, and these are at the same potential as the p^+ and n^+ end regions, respectively. Hence, the structure appears as a single inter-digitated p-n junction. As a result, when a reverse bias is applied between the p^+ and n^+ regions, this potential difference will appear across every p-n heterojunction, thus increasing the space-charge width on either sides of the hetero-interfaces. This is as shown in Fig. 14b. As the reverse bias is further increased, the p- and n-regions will eventually get completely depleted. Any further voltage increase beyond this point will only add a constant electric field parallel to the length L of the layers. This field can then be increased to values at which avalanche multiplication can take place.

The photodetector operation is illustrated more clearly in Fig. 15 which shows the energy-band diagram of the proposed device under operating conditions. The valence-band discontinuity has been assumed to be negligible. Suppose incident radiation is absorbed in the lower bandgap layer (InAs), thus creating electron-hole pair(s). The two p-n heterojunctions formed at the interfaces will serve to confine the electrons within the narrow bandgap layers, while sweeping holes out to the higher bandgap layers with subsequent confinement. The parallel field will cause electrons in the narrow bandgap layer to impact ionize. Holes generated, as a result, will be swept out before undergoing any impact ionization process. Thus, electrons and holes will be confined to different regions/layers, and only the electrons will predominantly ionize.

(b) A Staircase Avalanche Photodiode:

The idea of attaining strong differential impact ionization rates between electrons and holes for noise suppression can also be created by utilizing "staircase avalanche structures", as originally proposed by Matsuo et al. [69]. Fig. 16 shows the energy band diagram of such a staircase avalanche photodetector under un-biased and biased conditions. Valence band steps are assumed negligible. Consequently, holes do not impact ionize and only electrons can multiply during their transit. This elimination of hole initiated impact ionization, eliminates the feedback noise associated with conventional two-carrier avalanche devices. Furthermore, since electron multiplication can only occur at specific locations within the device, the unpredictability and statistical variability is virtually eliminated. The small values for the valence band steps can be achieved through a judicious selection of the Gallium mole fraction within InGaAs material.

(c) Case for $In\,As_x P_{1-x-y} Sb_y$ Photodetectors:

Finally, a case can be made for the use of $In\,As_x P_{1-x-y} Sb_y$-InAs photodiodes. The external quantum efficiency of InAs diodes tends to be limited to about 36 % due to the relatively high background doping which results in low lifetimes for the photogenerated carriers. The use of variable mole fractions will give rise to wavelength tenability, and such photodetectors can be used for the 1.0 – 3.8 μm range [70].

V. RELATED SUMMARY AND CONCLUSIONS

In conclusion, a simulation study for the transport properties of bulk InAs have been carried out for possible single-photon avalanche photo-detector applications. Such detection is of interest, especially at the 2 μm range for space applications. InAs material was chosen for a simulation study due to the following reasons. Its Γ–valley electronic effective mass of 0.022 m_o is one of the lowest and smaller than that of GaAs by a factor of 3. The inter-valley separation, however, is much larger than GaAs. Collectively then, a much better transient transport characteristics, leading to superior high-frequency operation and faster response are expected, as compared to GaAs. Furthermore, the possibility of using InGaAs alloys raises the possibility for wavelength tunability through bandgap engineering, and the formation of heterostructures and superlattices for producing precise shifts in the electronic states.

Currently, there are not many reports on the transient behavior or drift velocity-field characteristics for bulk InAs. Here, rigorous calculations based on the Monte Carlo method have been carried out. The model included details of the scattering mechanisms, impact ionization, dead-space and memory effects. Studies in InGaAs were discounted due to the inferior transport characteristics that are expected as the result of inherent alloy scattering. Our results for InAs, show that the transient drift velocities are significantly higher than the corresponding values for GaAs. This arises from much stronger velocity overshoot associated with k-space transfers. This bodes well for high-frequency photodetection. An analytical expression for the velocity-field characteristics was also obtained. This would be useful for device modeling and future InAs-based simulation work.

Avalanche multiplication behavior and related excess noise factors were also computed as a function of device length and applied voltage. The threshold electric field was shown to roughly scale up with decreasing device length due to the dead-space effect. The total avalanche voltages for devices of varying lengths (at least for the 0.4 – 10 μm regime shown), were all roughly comparable and underscore the total energy gain requirement for carrier multiplication as opposed to a dependence on the local electric field. From this standpoint alone, the device dimension does not appear to be a critical design parameter in enhancing the degree of avalanche multiplication for a given external bias. The transient transport results, however, suggest an inherent disadvantage to very long devices since, the small effective mass, Γ–valley conduction would no longer be dominant. Analysis of the excess noise behavior, suggests a decrease in F with increases in the device dimension. This is in keeping with the expectations of a non-local theory with with the electronics being dictated by a finite number of discrete collisions. However, it should be noted that scaling up the device lengths to reduce noise, might come at the expense of increased "dark currents". Field assisted detrapping and carrier generation, effects that have not been considered here. Thus, a moderate (and intermediate) range for the device dimensions, seem an optimal solution. In any case, the results here advocate the utility of InAs as an effective material for high-speed, high-frequency optical detectors at 2 μm.

The dark current response was also evaluated. The role of the various components has been analyzed. For shorter devices, the tunneling component is shown to dominate at low temperatures. Finally, possible structures for enhanced photodetection are proposed for future research.

VI. TANGIBLE OUTPUT FROM FUNDED PROJECT

(i) Research paper in an international peer-reviewed journal. Details: R. P. Joshi, G. Satyanadh, N. Abedin, and U. Singh, "Monte Carlo Calculation of Electron Drift Characteristics and Avalanche Noise in Bulk InAs", accepted for publication, Journal of Applied Physics, to appear 2002.

(ii) Research paper submitted to an international peer-reviewed journal. Details: R. P. Joshi, G. Satyanadh, N. Abedin, and U. Singh, "Monte Carlo Calculations of the Impulse Response in Bulk InAs for Single-Photon Avalanche Detection at 2 μm Wavelengths", Electronics Letters, submitted November 2002.

(iii) One graduate student thesis. Details: G. Satyanadh, M.S. student, thesis title: "Simulations of InAs Based Photodetectors for Single Photon Applications".

REFERENCES

1. O. Madelung, in *Physics of Group IV Elements and III-V Compounds*, Group III, Vols. 17a and 22a, Landolt-Bornstein New Series (Springer-Verlag, Berlin, 1981).
2. R. E. Nahory, M. A. Pollack, W. D. Johnson Jr., and R. L. Barns, Appl. Phys. Lett. **33**, 659 (1978).
3. D. Richards, J. Wagner, and J. Schmitz, Solid St. Commun. **100**, 7 (1996).
4. D. Schneider, C. Brink, G. Irmer, and P. Verma, Physica B **256-258**, 625 (1998).
5. C. Herman and C. Weibuch, Phys. Rev. B **15**, 823 (1977).
6. P. Verma, S. C. Abbi, and K. P. Jain, Phys. Rev. B **51**, 16660 (1995).
7. U. Kunze and W. Kowalsky, Appl. Phys. Lett. **53**, 367 (1988).
8. C. G. Bailey, M. Y. Yen, B. F. Levine, K. K. Choi, and A. Y. Cho, Appl. Phys. Lett. **51**, 1431 (1987).
9. W. Dobbelaere, W. D. Raedt, J. D. Boeck, R. Mertens, and G. Borghs, Electr. Lett. **28**, 372 (1992).
10. M. K. Parry and A. Krier, Electr. Lett. **30**, 1968 (1994).
11. B. D. Liu, R. M. Lin, S. C. Lee, and T. P. Sun, J. Vac. Sci. Technol. **B15**, 321 (1997).
12. H. Fujisada and T. Sasase, Jpn. J. Appl. Phys. **23**, 253 (1984).
13. A. Krier, Appl. Phys. Lett. **56**, 2428 (1990).
14. M. K. Parry and A. Krier, Semicond. Sci. Technol. **8**, 1764 (1993).
15. S. Belogurov, G. Bressi, G. Carugno, E. Conti, D. Iannuzzi, and A. T. Meneguzzo, Nuclr. Instr. Meth. **A 452**, 377 (2000).
16. T. F. Refaat, G. E. Halama, and R. J. DeYoung, Optical Engineering **39**, 2642 (2000).
17. A. Spinelli, L. M. Davis, and H. Dautet, Rev. Sci. Instrum. **67**, 55 (1996).

18. H. Dautet, P. Deschamps, B. Dion, A. D. MacGregor, D. MacSween, R. J. McIntyre, C. Trottier, and P. P. Webb, Appl. Optics **32**, 3894 (1993).
19. J. G. Rarity, T. E. Wall, K. D. Ridley, P. C. Owens, and P. R. Tapster, Applied Optics **39**, 6746 (2000).
20. R. G. W. Brown, R. Jones, J. G. Rarity, and K. D. Ridley, Appl. Optics **26**, 2383 (1987).
21. K. Nishida, K. Taguchi, and Y. Matsumoto, Appl. Phys. Lett. **35**, 251 (1979).
22. J. C. Campbell, A. G. Dentai, W. S. Holden, and B. L. Kasper, Electr. Lett. **18**, 818 (1983) ; H. Nie, K. A. Anselm, C. Hu, S. S. Murtaza, B. G. Streetman, and J. C. Campbell, Appl. Phys. Lett. **70**, 161 (1997).
23. L. E. Tarof, J. Yu, R. Bruce, D. G. Knight, T. Baird, and B. Oosterbrink, IEEE Photonics Technol. Lett. **PTL-5**, 672 (1993).
24. R. J. McIntyre, IEEE Trans. Electr. Dev **ED-13**, 164 (1966).
25. K. M. Van Vliet, A. Friedmann, and L. M. Rucker, IEEE Trans. Electr. Dev **ED-26**, 752 (1979).
26. C. Hu, K. A. Anselm, B. G. Streetman, and J. C. Campbell, Appl. Phys. Lett. **69**, 3734 (1996).
27. W. A. Lukaszek, A. van der Ziel, and E. R. Chenette, Solid State Electr. **19**, 57 (1976).
28. K. M. van Vliet, A. Friedmann, and L. M. Rucker, IEEE Trans. Electr. Dev. **ED-26**, 752 (1979).
29. J. S. Marsland, J. Appl. Phys. **67**, 1929 (1990) ; J. S. Marsland, R. C. Woods, and C. A. Brownhill, IEEE Trans. Electr. Dev. **ED-39**, 1129 (1992).
30. B. K. Ridley, J. Phys. C **16**, 3373 (1983).
31. B. E. A. Saleh, M. M. Hayat, and M. C. Teich, IEEE Trans. Electr. Dev. **ED-37**, 1976 (1990).
32. D. S. Ong, K. F. Li, G. J. Rees, J. P. David, P. N. Robson, and G. M. Dunn, Appl. Phys. Lett. **72**, 232 (1998) ; D. S. Ong, K. F. Li, S. A. Plimmer, G. J. Rees, J. P. David, and P. N. Robson, J. Appl. Phys. **87**, 7885 (2000).
33. For example, R. P. Joshi, J. Appl. Phys. **78**, 5518 (1995), and references therein.
34. P. Damayanthi, R. P. Joshi, and J. A. McAdoo, J. Appl. Phys.**86**, 5060 (1999).
35. M. Costato, C. Jacoboni, and L. Reggiani, Phys. Stat. Solidi B **52**, 461 (1972) ; S. Bosi, C. Jacoboni, and L. Reggiani, J. Phys. C **12**, 1523 (1979).
36. D. Kranzer, Phys. Stat. Solidi A **26**, 11 (1974) ; D. Kranzer, J. Phys. C: Solid State Physics **6**, 2967 (1973).
37. M. A. Osman and D. K. Ferry, Phys. Rev. B **36**, 6018 (1987).
38. B. Lax and J. G. Mavroides, Phys. Rev. **100**, 1650 (1955) ; J. G. Mavroides and B. Lax, Phys. Rev. **107**, 1530 (1957).
39. E. O. Kane, J. Phys. Chem. Solids **1**, 249 (1957).
40. G. Dresselhaus, Phys. Rev. **100**, 580 (1955).
41. J. Robert, B. Pistoulet, D. Barjon, and A. Raymond, J. Phys. Chem. Solids **34**, 2221 (1973).
42. F. Matossi and F. Stern, Phys. Rev. **111**, 472 (1958).
43. W. Shockley, Solid State Electr. **2**, 35 (1961).
44. P. A. Wolff, Phys. Rev. **95**, 1415 (1954).
45. G. A. Baraff, Phys. Rev. **128**, 2507 (1962).
46. A. R. Beattie and P. T. Landsberg, Proc. R. Soc. London Ser. **A 249**, 16 (1958).

47. E. O. Kane, Phys. Rev. **159**, 159 (1967).
48. D. J. Robbins, Phys. Stat. Sol. **B 97**, 9 (1980) ; D. J. Robbins, Phys. Stat. Sol. **B 97**, 387 (1980).
49. H. Shichijo and K. Hess, Phys. Rev. B **23**, 4197 (1981).
50. Y. Wang and K. F. Brennan, J. Appl. Phys. **71**, 2736 (1992).
51. R. Thoma, H. J. Peifer, W. L. Engl, W. Quade, R. Brunetti, and C. Jacoboni, J. Appl. Phys. **69**, 2300 (1991).
52. M. Fischetti and S. Laux, Phys. Rev. **B 38**, 9721 (1988).
53. V. Keldysh, Sov. Phys. JETP **21**, 1135 (1965).
54. R. Brunetti, C. Jacoboni, and F. Rossi, Phys. Rev. **B 39**, 10781 (1989).
55. W. Quade, E. Scholl, and M. Ruden, Solid State Electr. **36**, 1493 (1993).
56. E. Scholl and W. Quade, J. Phys. C **20**, L861 (1987).
57. A. Di Carlo, P. Vogl, and W. Potz, Phys. Rev. B **50**, 8358 (1994).
58. B. K. Ridley and T. B. Watkins, Proc. Phys. Soc. Lond. **78**, 293 (1961).
59. C. Hilsum, Proc. IRE **50**, 185 (1962).
60. Y. Hori, Y. Ando, Y. Miyamoto, and O. Sugino, Solid St. Electr. **43**, 1813 (1999).
61. V. Souw, V. Gopal, E.-H. Chen, E. P. Kvam, M. McElfresh, and J. M. Woodall, Appl. Phys. Lett. **77**, 1176 (2000) ; V. Gopal, V. Souw, E. -H. Chen, E. P. Kvam, M. McElfresh, and J. M. Woodall, J. Appl. Phys. **87**, 1350 (2000).
62. C. Jacoboni, C. Canali, G. Ottoviani, and A. Alberigi-Quaranta, Solid St. Electr. **20**, 77 (1977).
63. T. J. Maloney and J. Frey, J. Appl. Phys. **48**, 781 (1977).
64. Y. K. Feng, Electr. Lett. **21**, 453 (1985).
65. Y. J. Jung, B. H. Kim, H. J. Lee, and J. C. Wolley, Phys. Rev. **26**, 3151 (1982).
66. C. H. Kuan, R. M. Lin, S. F. Tang, and T. P. Sun, J. Appl. Phys. **80**, 5454 (1996).
67. R. Chin, N. Holonyak, Jr., G. E. Stillman, J. T. Tang, and K. Hess, Electr. Lett. **16**, 467 (1980).
68. F. Capasso, Appl. Phys. Lett. **40**, 38 (1982) ; F. Capasso, IEEE Trans. Electr. Dev. **29**, 1388 (1982).
69. K. Matsuo, M. C. Teich, and B. E. A. Saleh, J. Lightwave Technol. **3**, 1223 (1985).
70. X. Y. Gong, T. Yamaguchi, H. Kan, T. Makino, T. Iida, T. Kato, M. Aoyama, Y. Hayakawa, and M. Kumagawa, Jpn. J. Appl. Phys. **36**, 2614 (1997).

Table I Parameters Used For Hole Transport In Bulk InAs

PARAMETER	VALUE
Lattice constant (m)	6.058×10^{-10}
Heavy hole effective mass (m^*_{HH})	0.41
Γ-valley effective mass (m^*_{Γ})	0.022
L-valley effective mass (m^*_{L})	0.5
Average sound velocity (cm/sec)	3.24×10^5
Density (g/cm^3)	5.667
Relative permittivity (High frequency)	12.3
Relative permittivity (Static)	15.15
Longitudinal elastic constant (dyn/cm^2)	1.0×10^{12}
Transverse elastic constant (dyn/cm^2)	3.55×10^{11}
Acoustic deformation potential (eV)	6.5
Nonpolar optical deformation potential (eV)	6.5
Longitudinal optical phonon energy (meV)	29.7
Transverse optical phonon energy (meV)	27.4
Effective interband phonon energy (meV)	30.2

FIGURE CAPTION

Fig. 1 The general energy-band diagram relevant to the impact ionization process. An electron initially in state $\mathbf{k}_1$ and band α makes a transition to state $\mathbf{k}_1'$ in band β, while the other participating electron in state $\mathbf{k}_2$ and band δ shifts to state $\mathbf{k}_2'$ in band γ.

Fig. 2 Results of the transient electron drift velocity in InAs obtained from Monte Carlo simulations at 300 K for different applied electric fields.

Fig. 3 Temporal variation of the Γ– and L-valley populations in InAs at electric fields of 0.5 kV/cm, 4 kV/cm, and 8 kV/cm.

Fig. 4 Predicted steady-state electron drift velocity versus field behavior of InAs at 300 K.

Fig. 5 Average multiplication factor as a function of the electric field in the intrinsic region for different device lengths.

Fig. 6 Histogram of the multiplication factor at 300 K for an electric field of 50 kV/cm and a 2 μm device length.

Fig. 7 Excess noise factor versus multiplication with the device length as the parameter.

Fig. 8 Calculated reverse dark current for a 0.14 μm p-i-n device as a function of the inverse temperature at a reverse bias of 1.0 Volt.

Fig. 9 Reverse dark current components for a 0.14 μm p-i-n device as a function of applied bias at 300 Kelvin.

Fig. 10 Calculated reverse dark current characteristics for a 1.0 μm p-i-n device. (a) Current variation with inverse temperature at a 1.0 Volt reverse bias, and (b) Current dependence on applied bias at 300 Kelvin.

Fig. 11 Monte Carlo results of the impulse response for 1.0 μm p-i-n avalanche detectors at 300 K. (a) Temporal evolution of the carrier populations for 10 kV/cm and 50 kV/cm fields, (b) Corresponding occupancy within the Γ- and L-valleys, and (c) the photocurrents versus time at the two electric fields.

Fig. 12 Monte Carlo results of the impulse response comparing 1.0 μm and 3.5 μm p-i-n avalanche detectors

at 300 K. (a) Temporal evolution of the carrier populations for a 10 kV/cm field, (b) Hole population versus time for the 3.5 μm device, and (c) the photocurrents versus time.

Fig. 13. Schematic of a proposed interdigitated, low-noise avalanche photodetector (APD).

Fig. 14 Cross section of the p-n junction device at different reverse bias settings. The shaded portions represent the depleted volumes.

Fig. 15 Energy-band diagram of the proposed APD under operating conditions. The valence-band discontinuity has been assumed to be negligible.

Fig. 16 Energy band diagram of a staircase avalanche photodetector under un-biased and biased conditions. Valence band steps are assumed negligible, and so holes do not impact ionize and only electrons multiply.

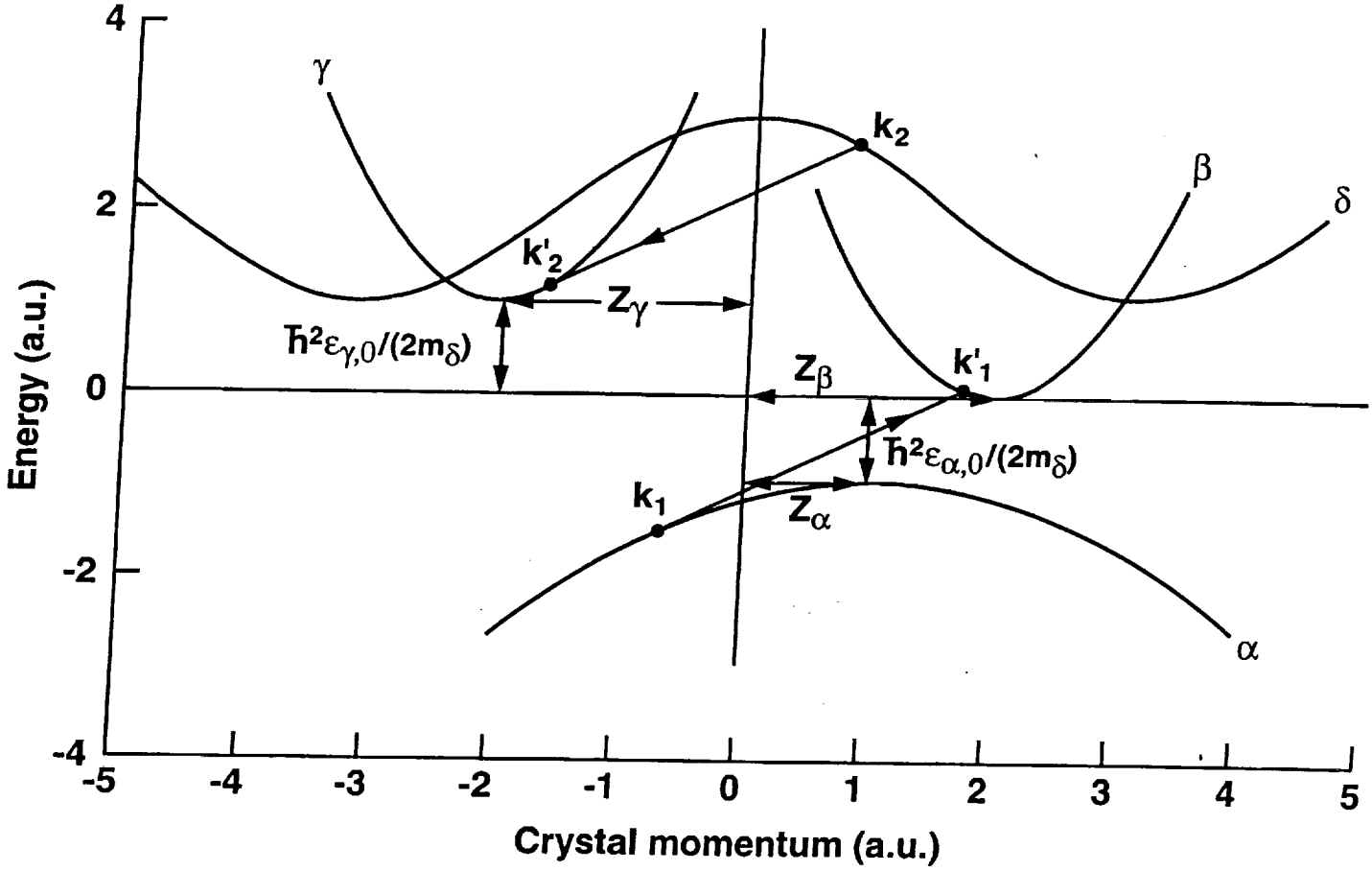

Fig. 1 The general energy-band diagram relevant to the impact ionization process. An electron initially in state $\mathbf{k}_1$ and band α makes a transition to state $\mathbf{k}_1'$ in band β, while the other participating electron in state $\mathbf{k}_2$ and band δ shifts to state $\mathbf{k}_2'$ in band γ.

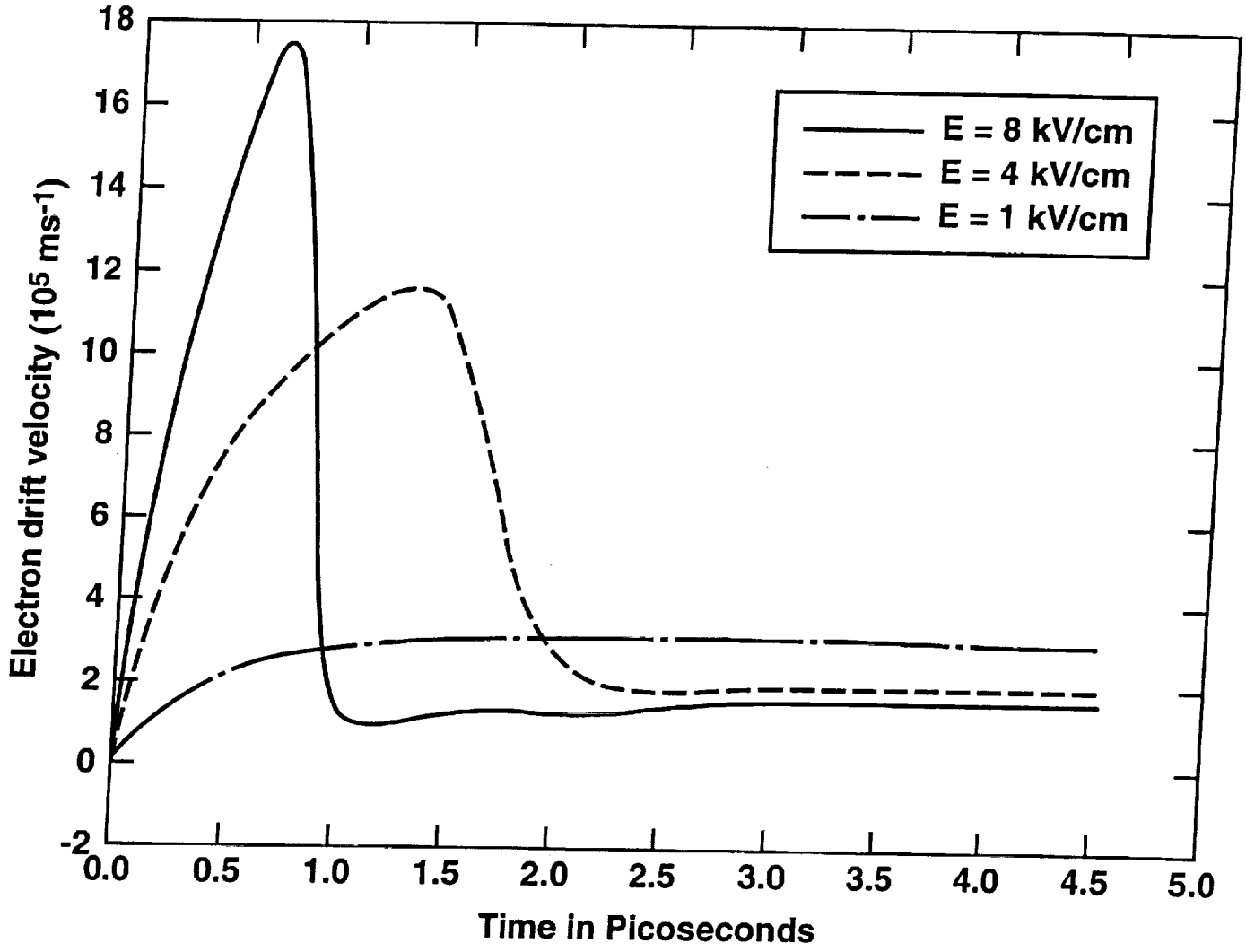

Fig. 2 Results of the transient electron drift velocity in InAs obtained from Monte Carlo simulations at 300 K for different applied electric fields.

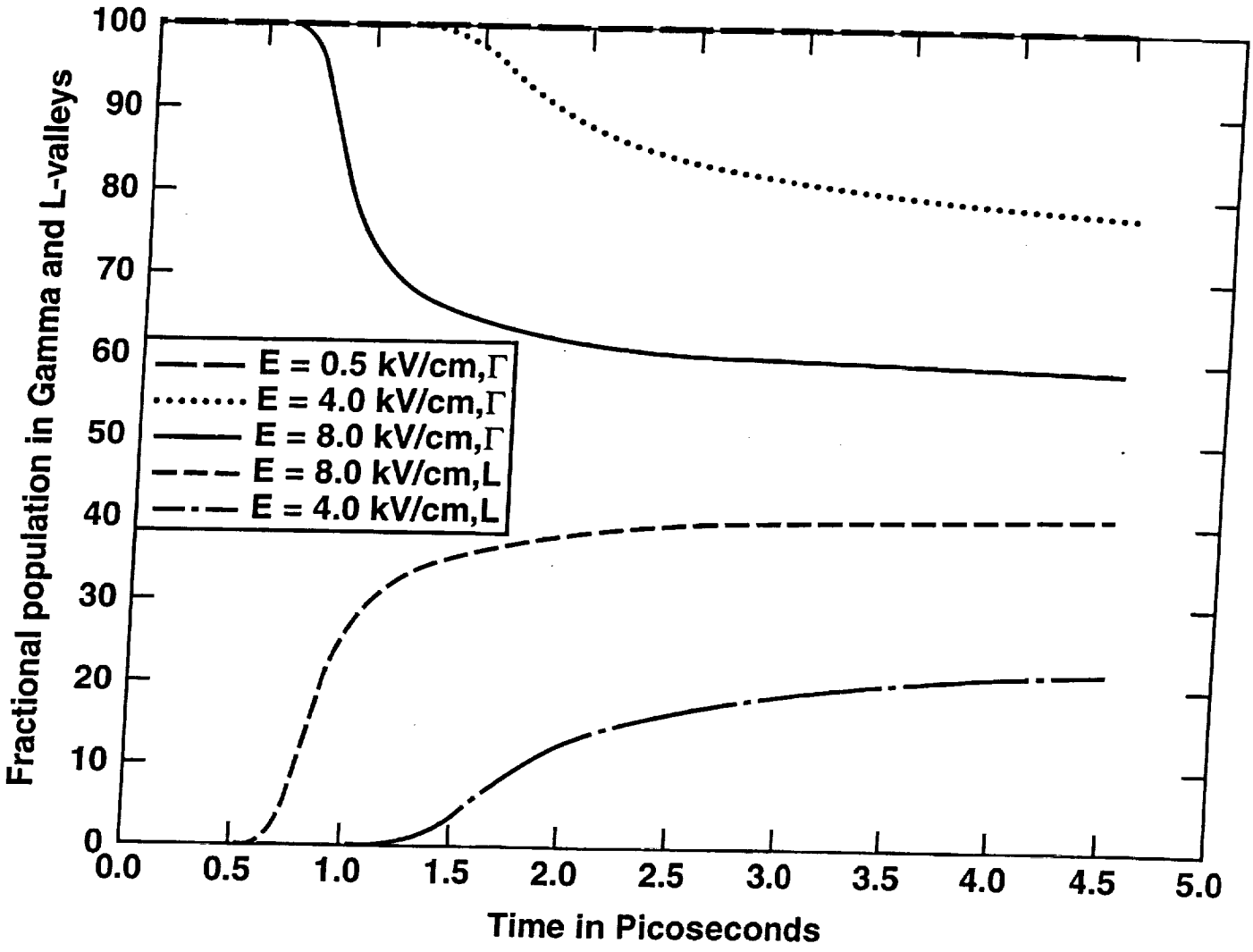

Fig. 3 Temporal variation of the Γ– and L-valley populations in InAs at electric fields of 0.5 kV/cm, 4 kV/cm, and 8 kV/cm.

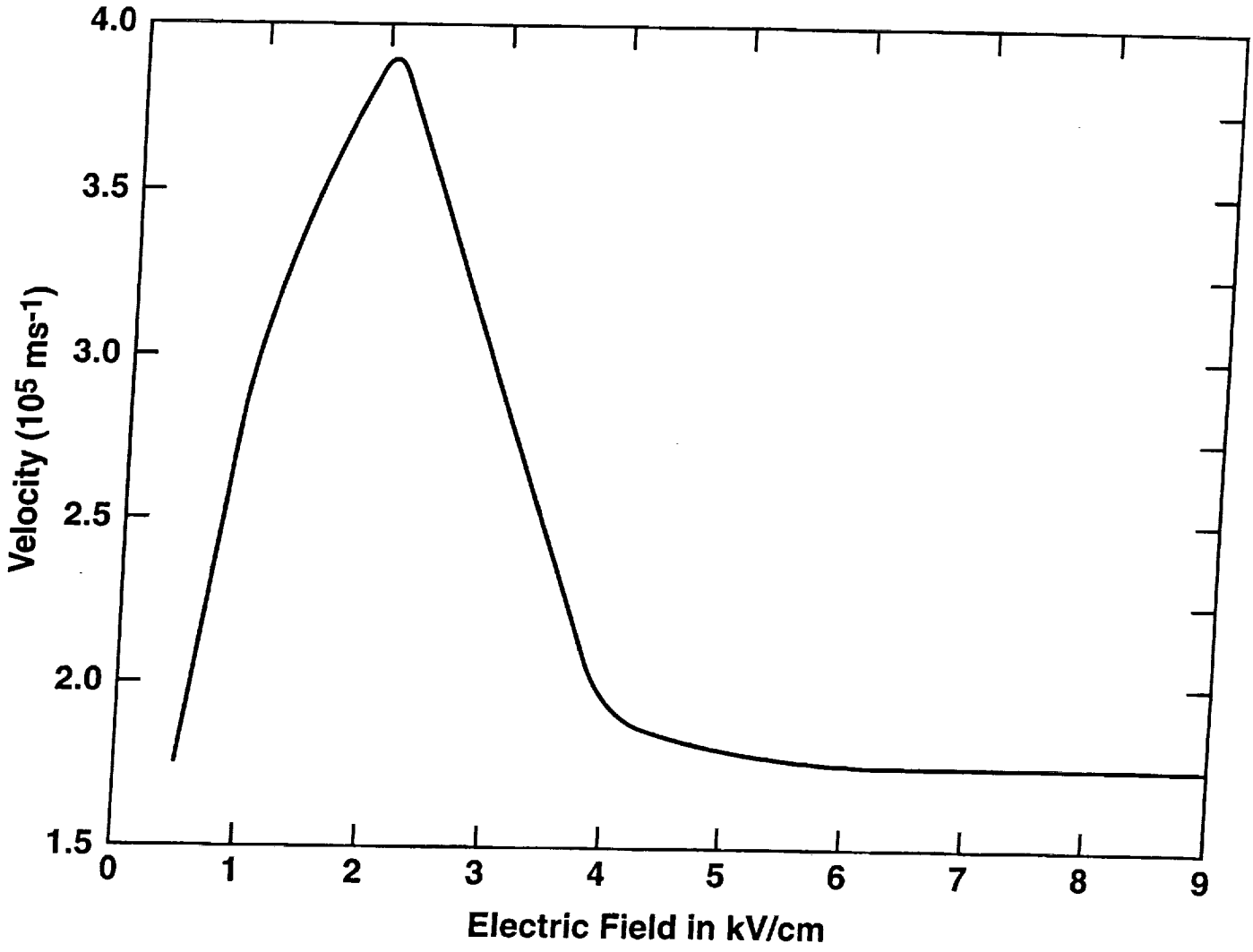

Fig. 4 Predicted steady-state electron drift velocity versus field behavior of InAs at 300 K.

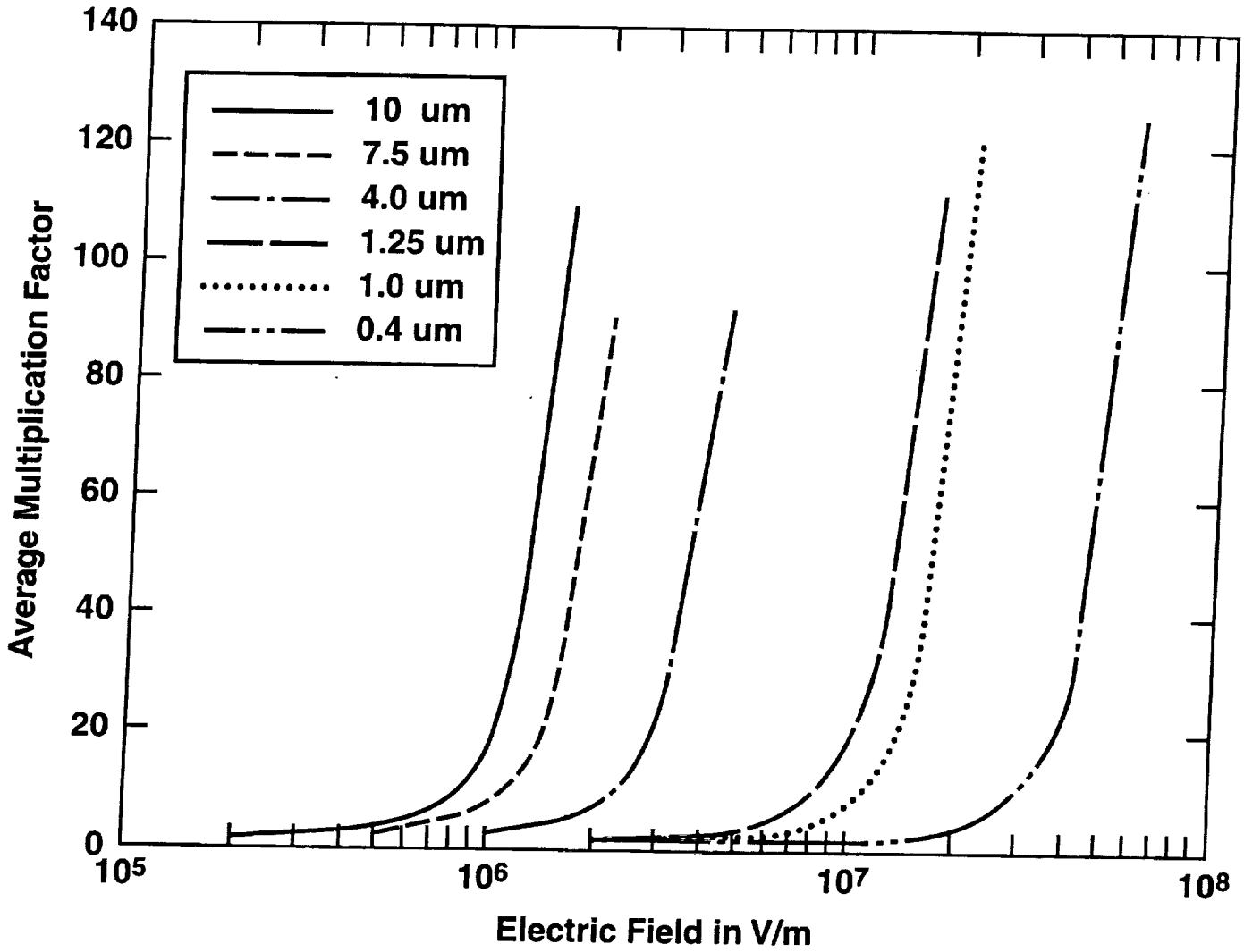

Fig. 5 Average multiplication factor as a function of the electric field in the intrinsic region for different device lengths.

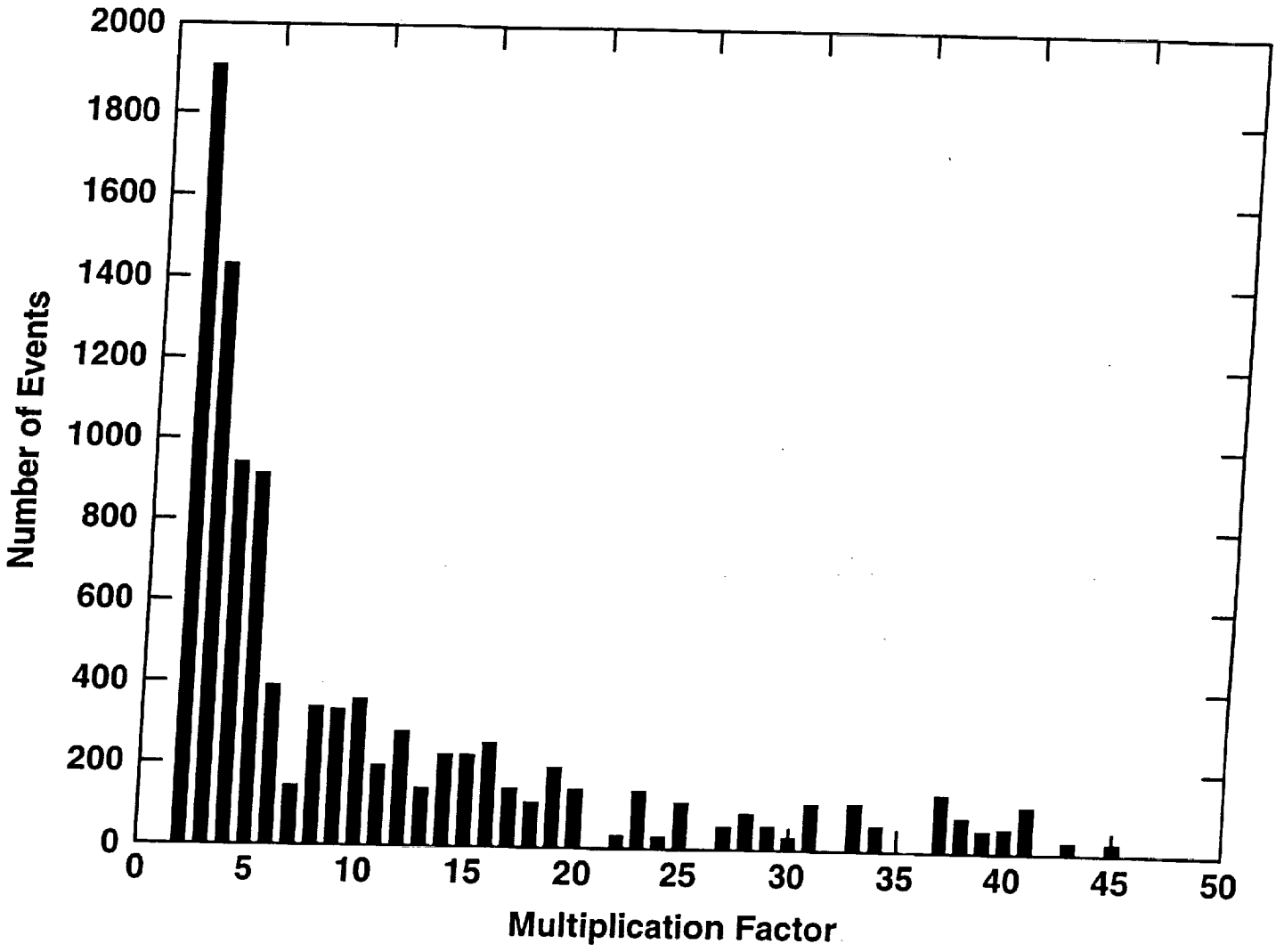

Fig. 6 Histogram of the multiplication factor at 300 K for an electric field of 50 kV/cm and a 2 μm device length.

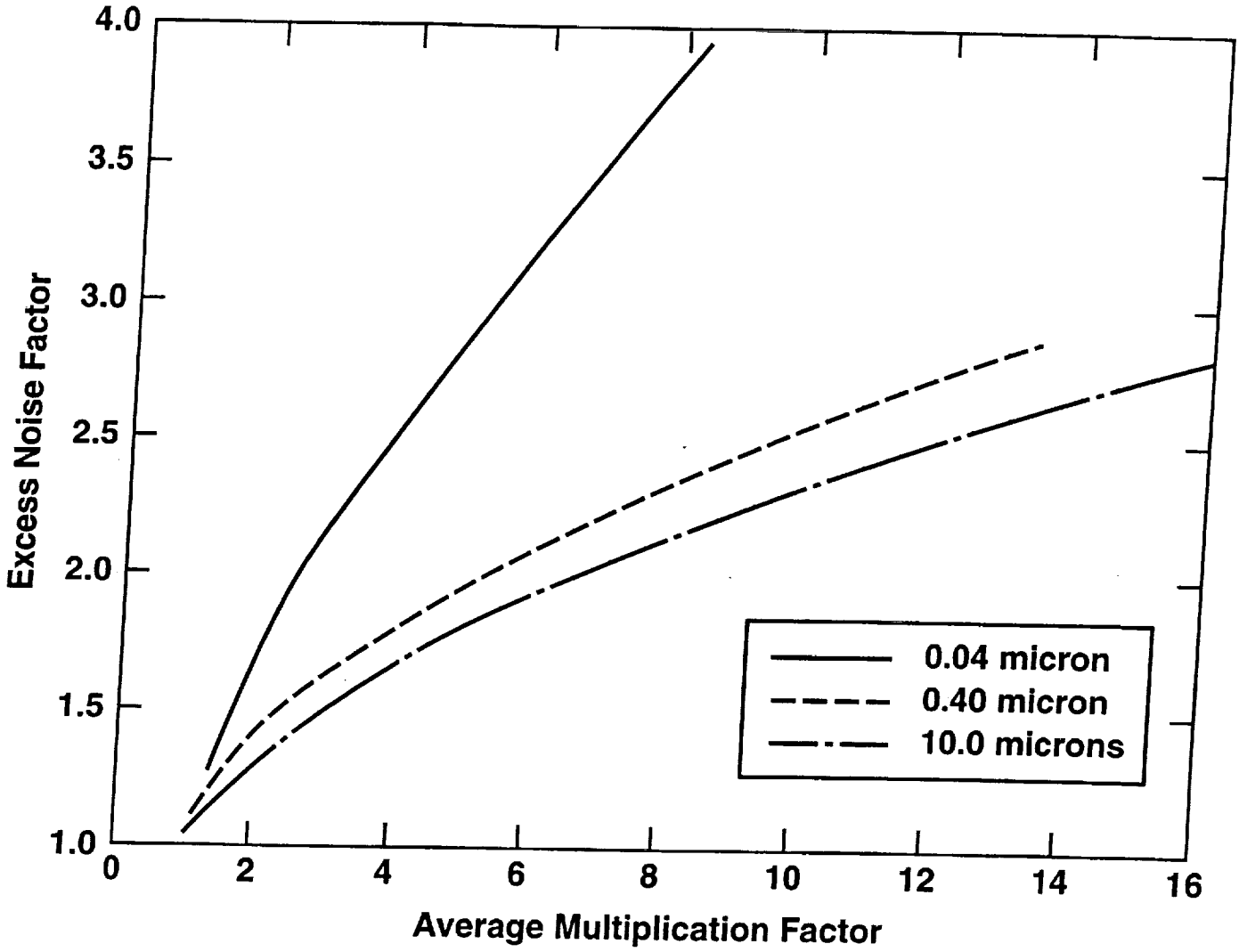

Fig. 7 Excess noise factor versus multiplication with the device length as the parameter.

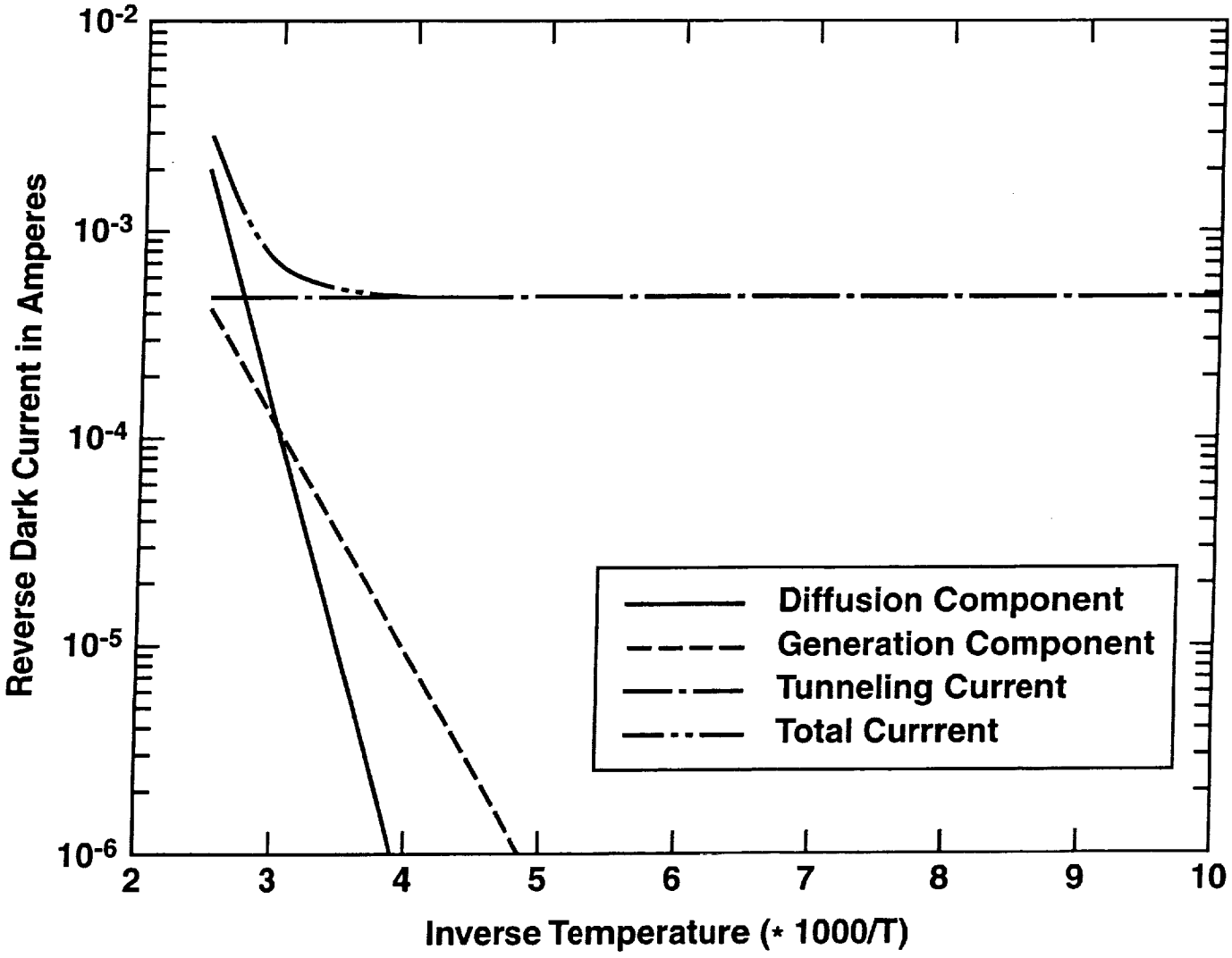

Fig. 8 Calculated reverse dark current for a 0.14 μm p-i-n device as a function of the inverse temperature at a reverse bias of 1.0 Volt.

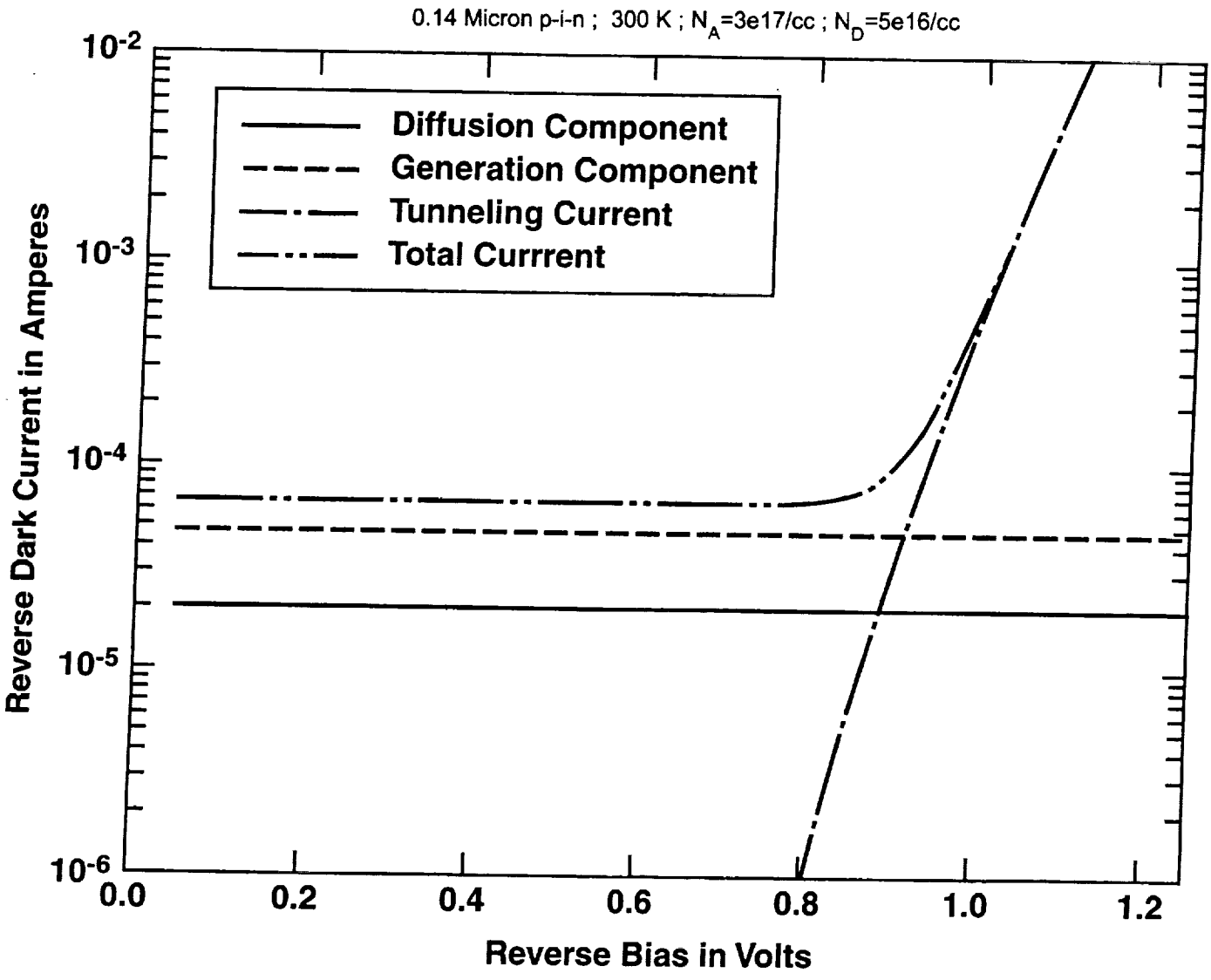

Fig. 9 Reverse dark current components for a 0.14 μm p-i-n device as a function of applied bias at 300 Kelvin.

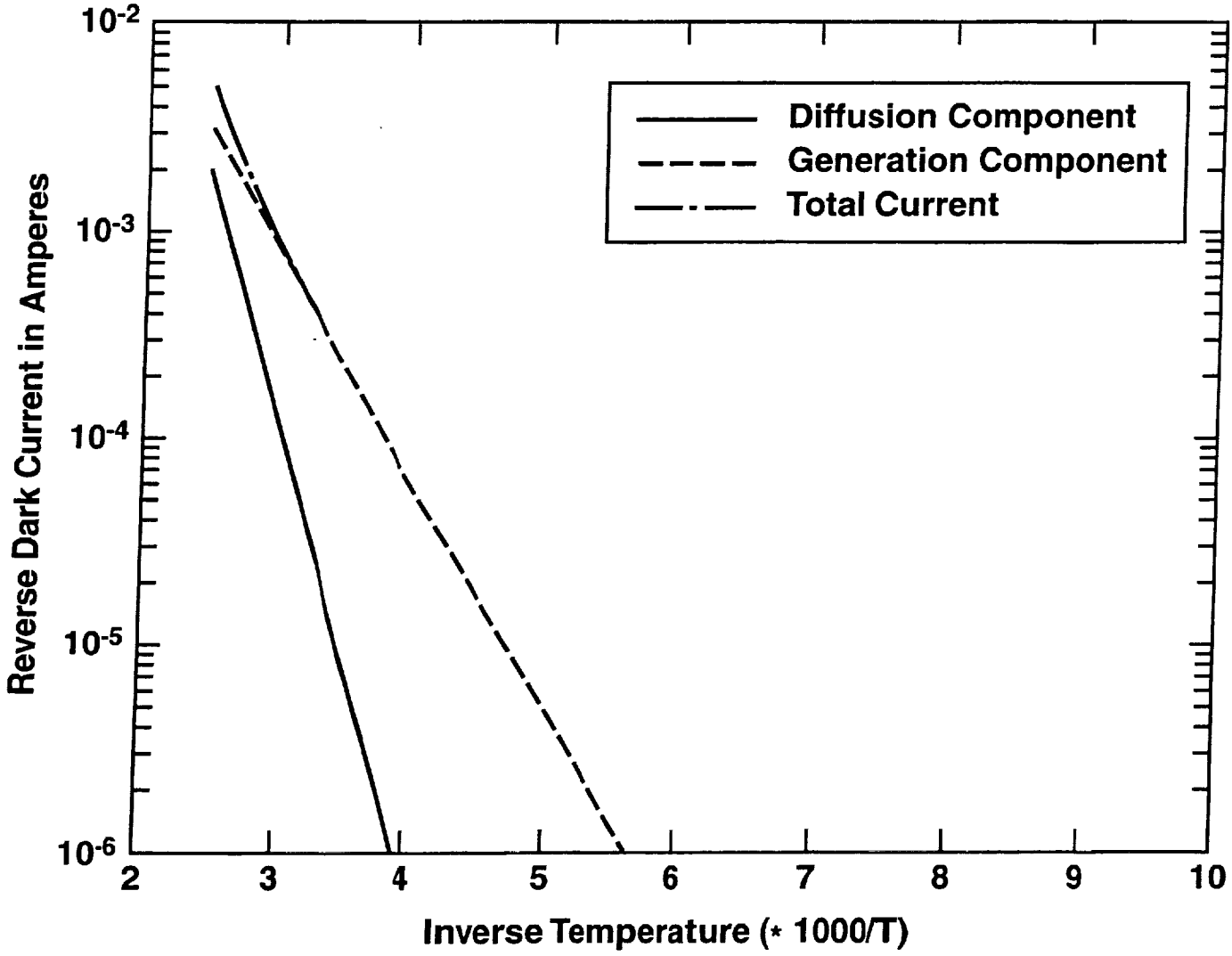

Fig. 10 (a) Calculated reverse dark current characteristics for a 1.0 μm p-i-n device. Current variation with inverse temperature at a 1.0 Volt reverse bias.

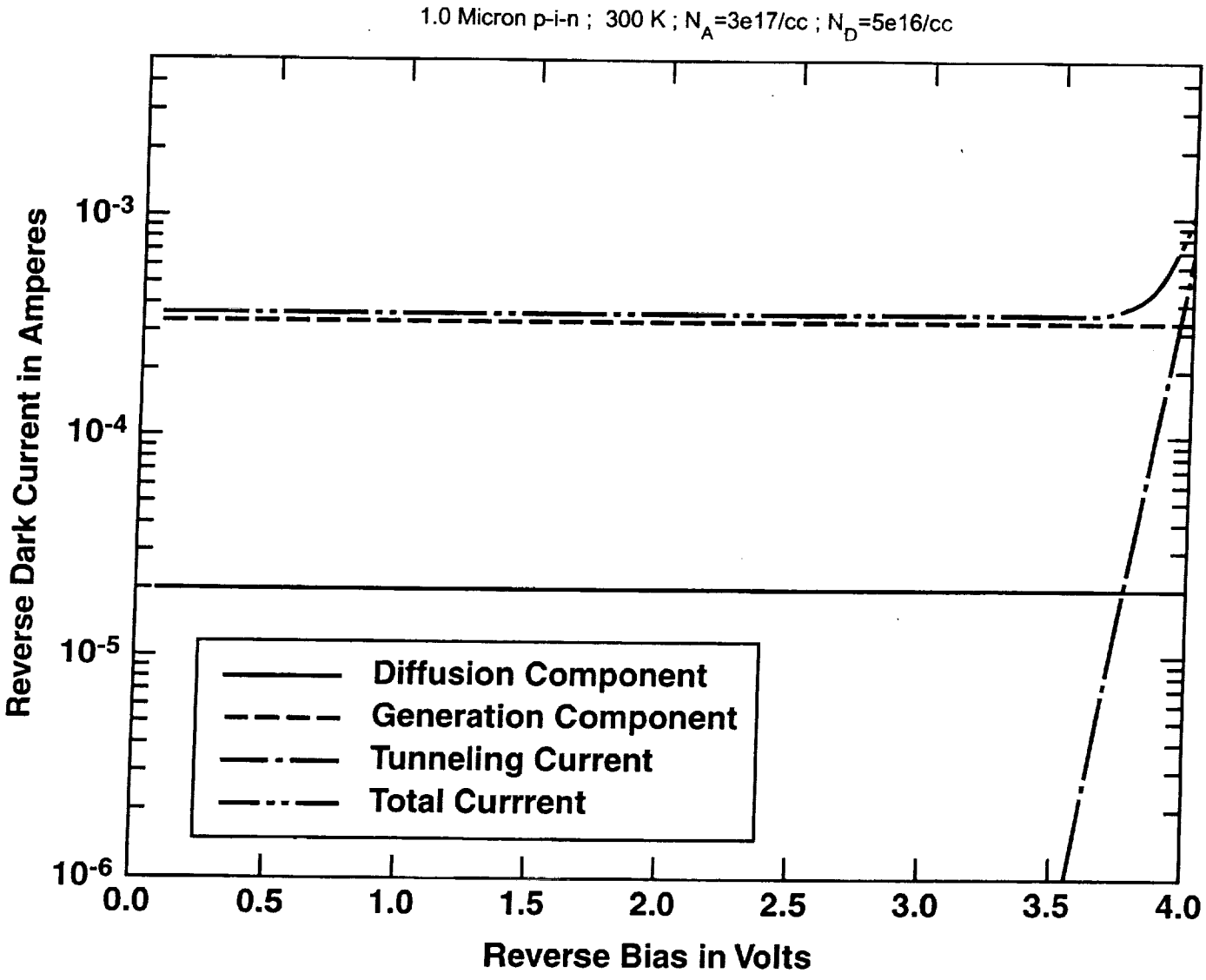

Fig. 10 (b) Calculated reverse dark current characteristics for a 1.0 μm p-i-n device. Current dependence on applied bias at 300 Kelvin.

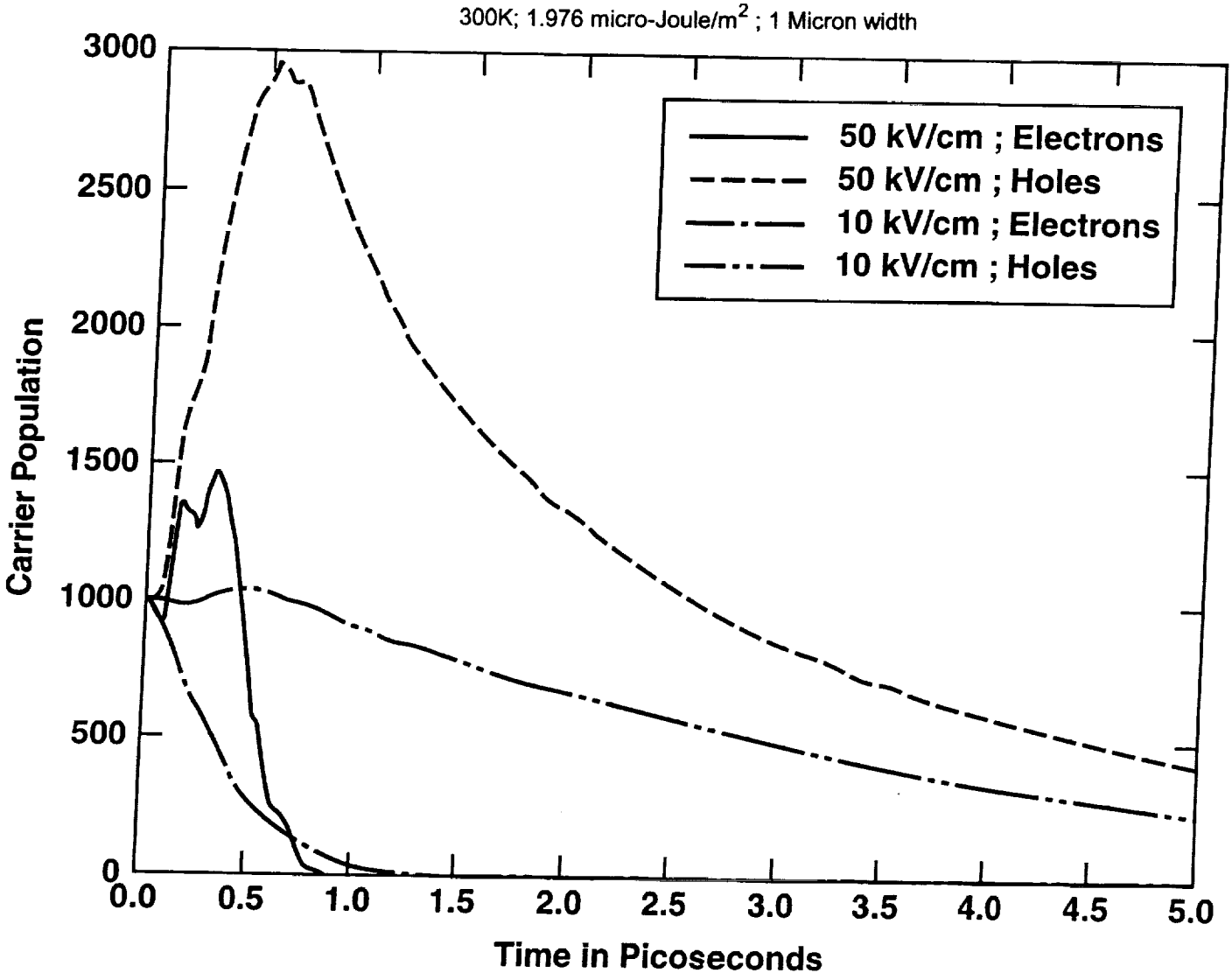

Fig. 11 (a) Monte Carlo results of the impulse response for 1.0 μm p-i-n avalanche detectors at 300 K. Temporal evolution of the carrier populations for 10 kV/cm and 50 kV/cm fields

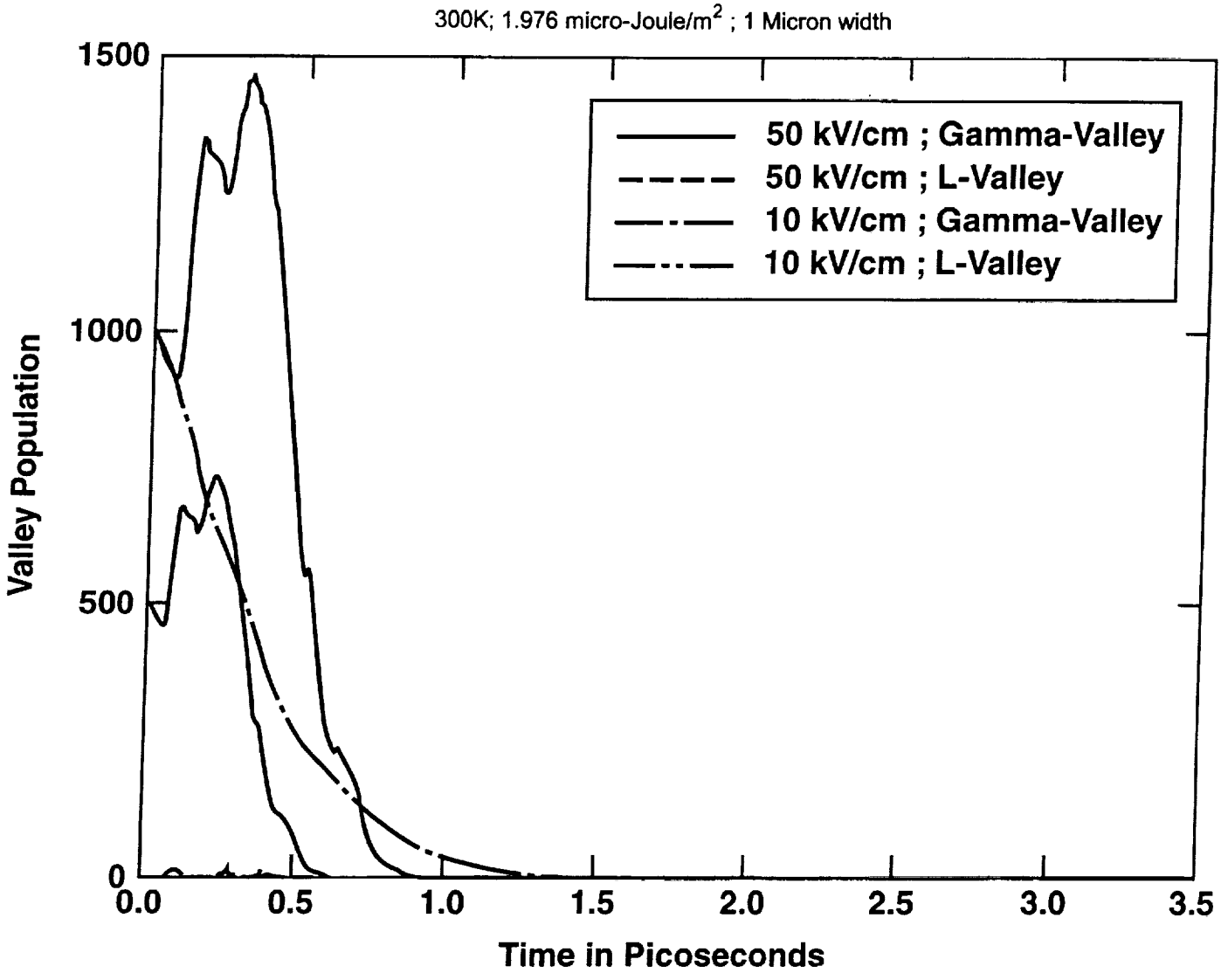

Fig. 11 (b) Monte Carlo results of the impulse response for 1.0 μm p-i-n avalanche detectors at 300 K. Corresponding occupancy within the Γ- and L-valleys.

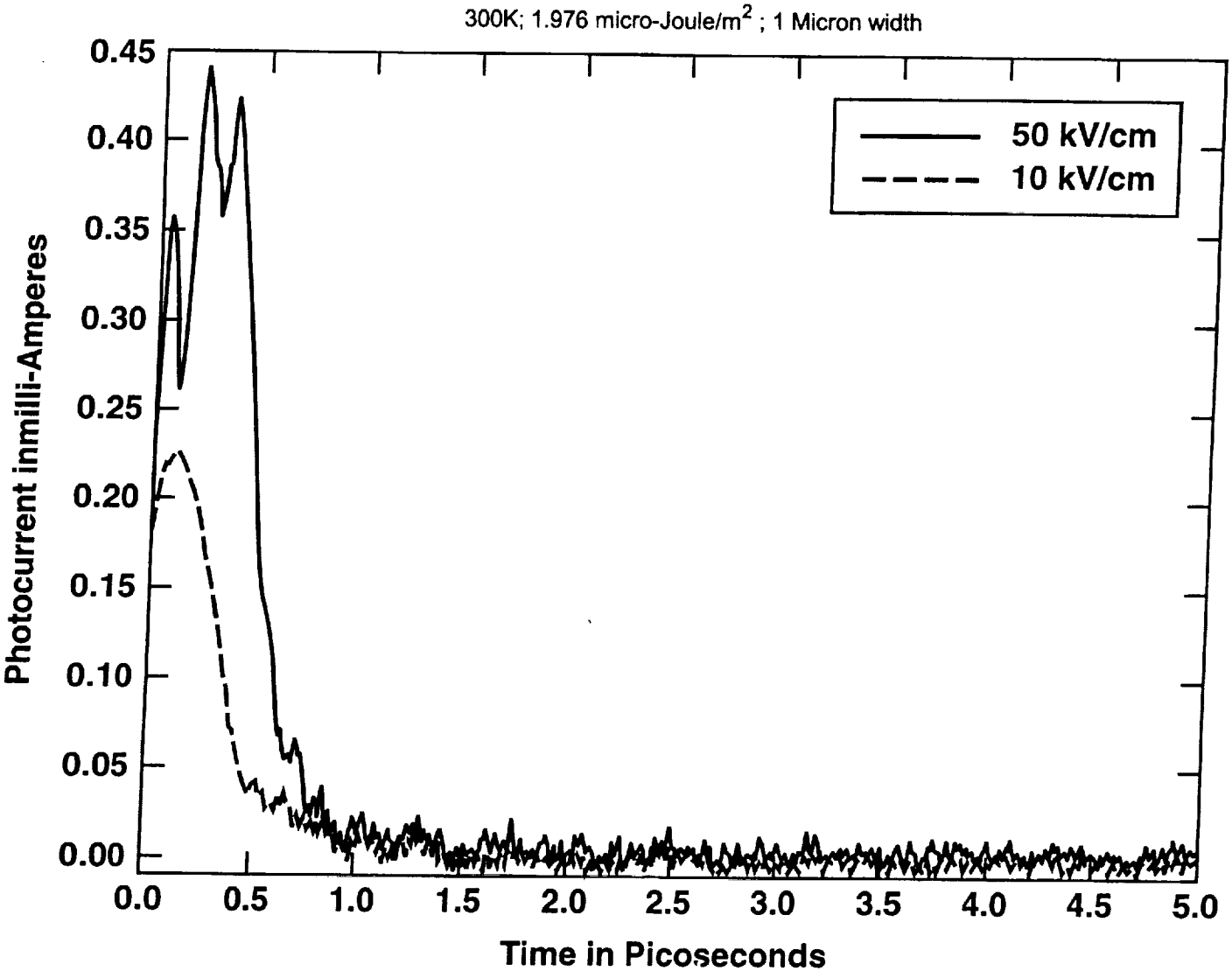

Fig. 11 (c) Monte Carlo results of the impulse response for 1.0 μm p-i-n avalanche detectors at 300 K. Photocurrents versus time at the two electric fields.

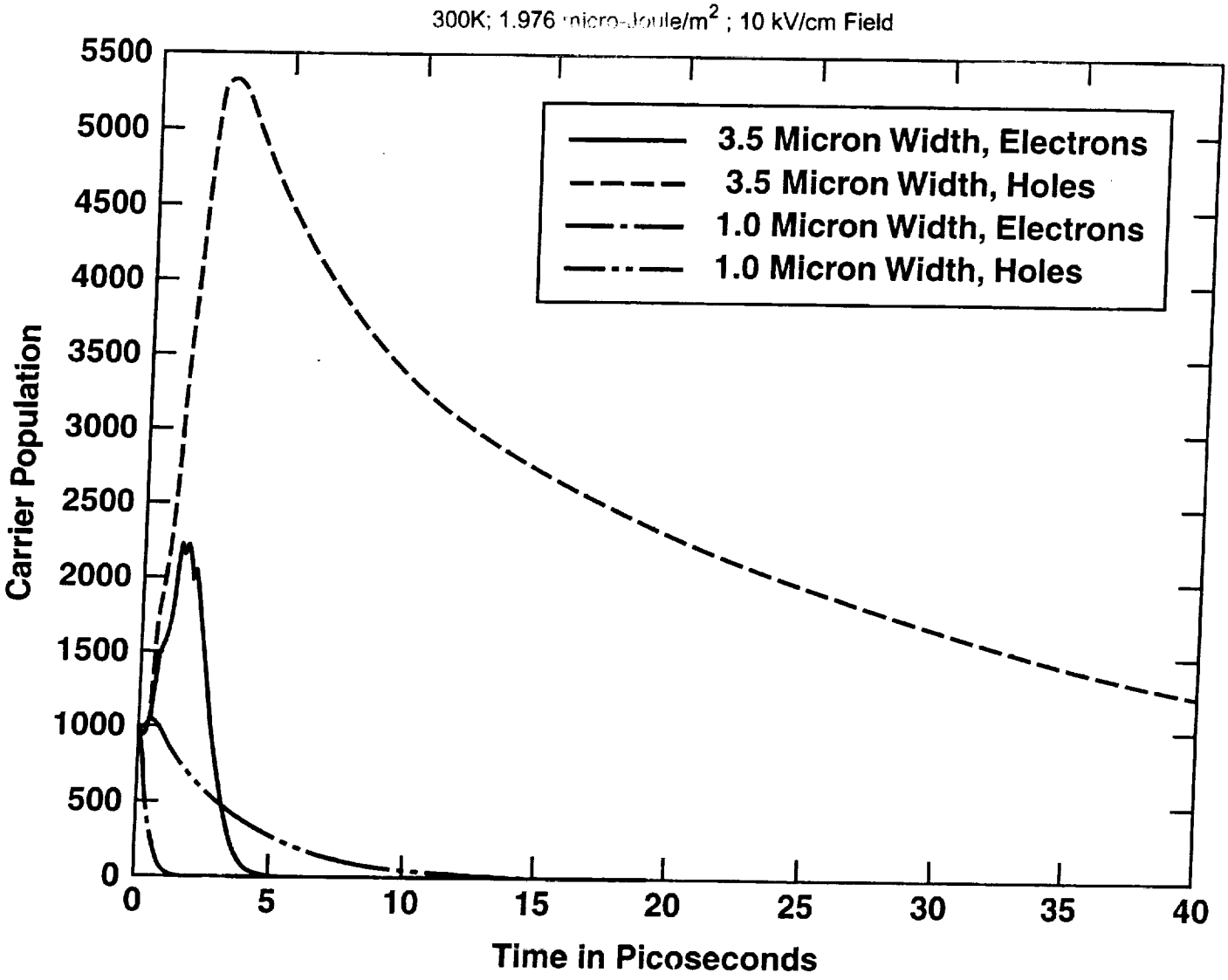

Fig. 12 (a) Monte Carlo results of the impulse response comparing 1.0 μm and 3.5 μm p-i-n avalanche detectors at 300 K. Temporal evolution of the carrier populations for a 10 kV/cm field.

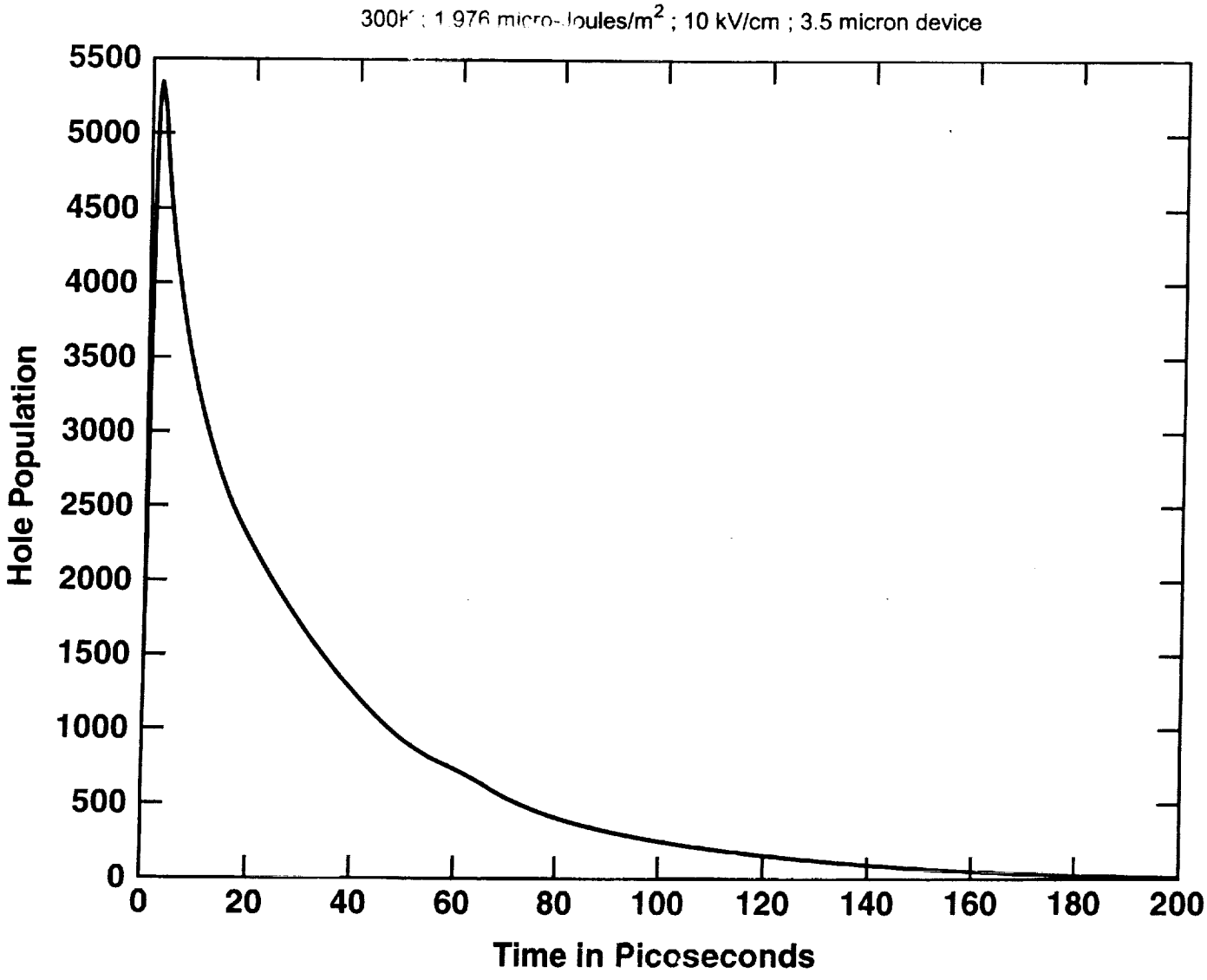

Fig. 12 (b) Monte Carlo results of the impulse response comparing 1.0 μm and 3.5 μm p-i-n avalanche detectors at 300 K. Hole population versus time for the 3.5 μm device .

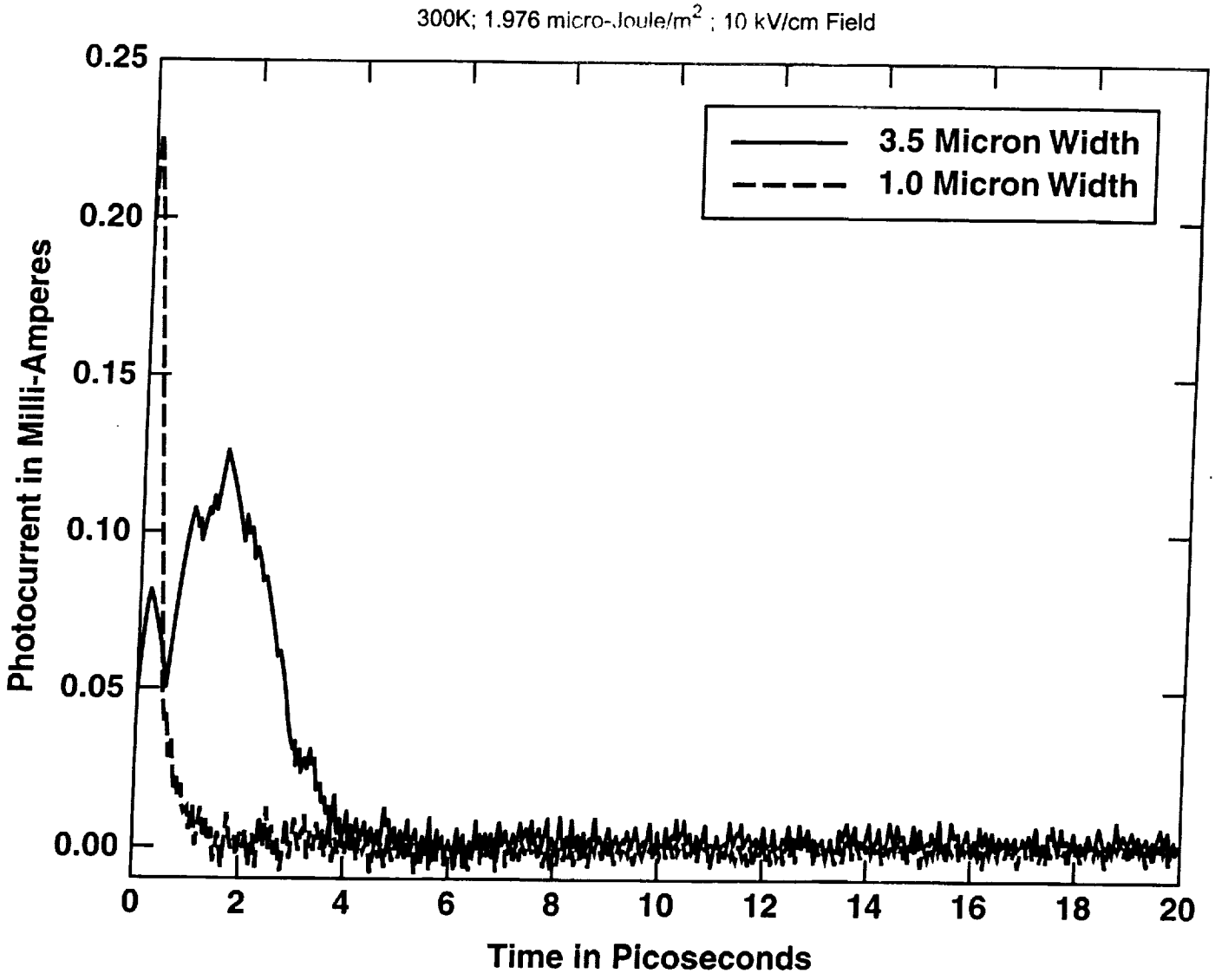

Fig. 12 (c) Monte Carlo results of the impulse response comparing 1.0 μm and 3.5 μm p-i-n avalanche detectors at 300 K. Photocurrents versus time.

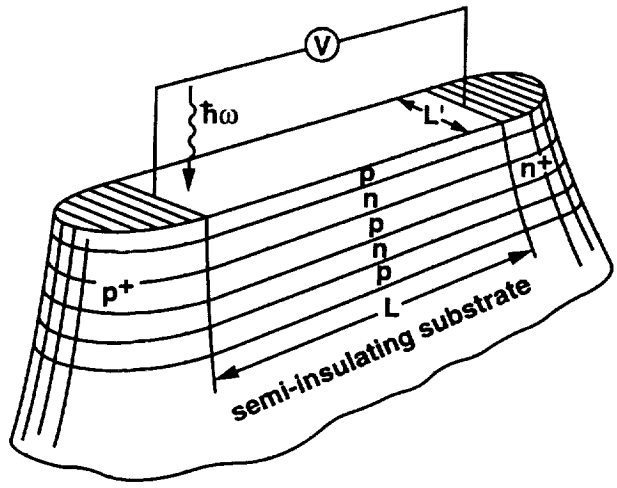

Fig. 13. Schematic of a proposed interdigitated, low-noise avalanche photodetector (APD).

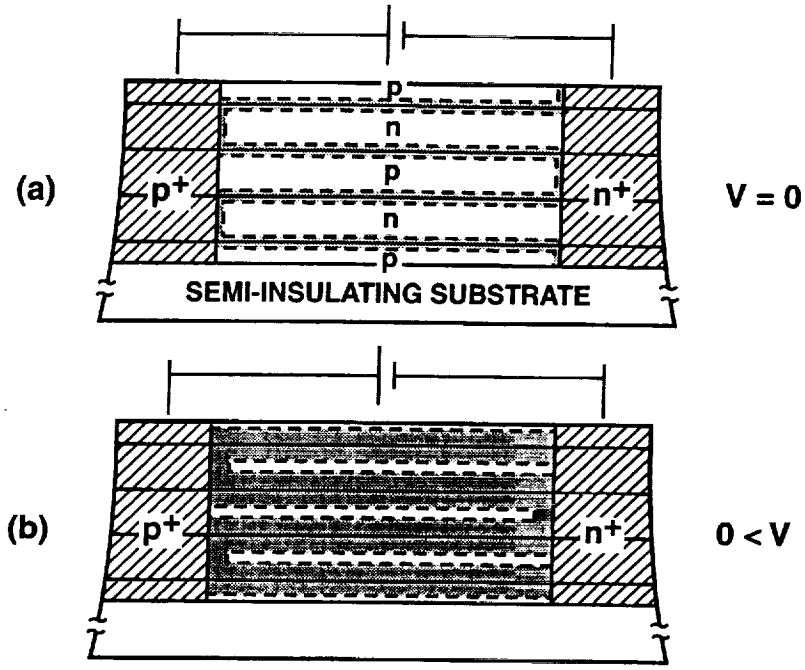

Fig. 14 Cross section of the p-n junction device at different reverse bias settings. The shaded portions represent the depleted volumes. (a) Zero applied voltage, and (b) Finite reverse bias.

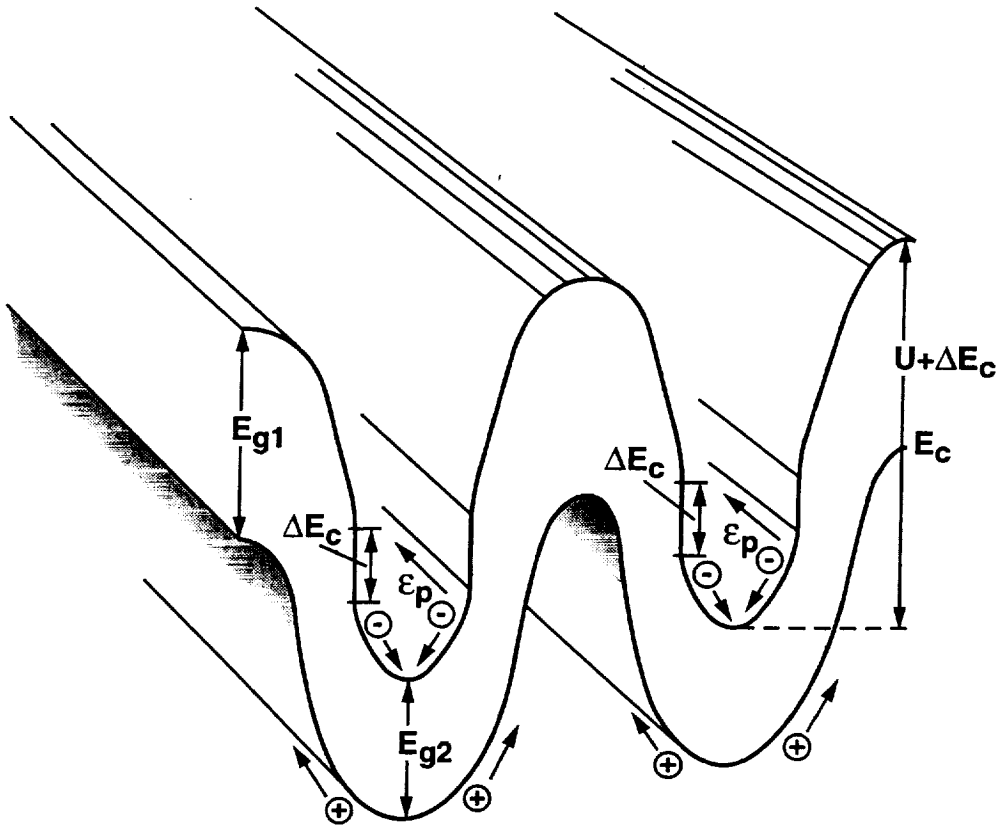

Fig. 15 Energy-band diagram of the proposed APD under operating conditions. The valence-band discontinuity has been assumed to be negligible.

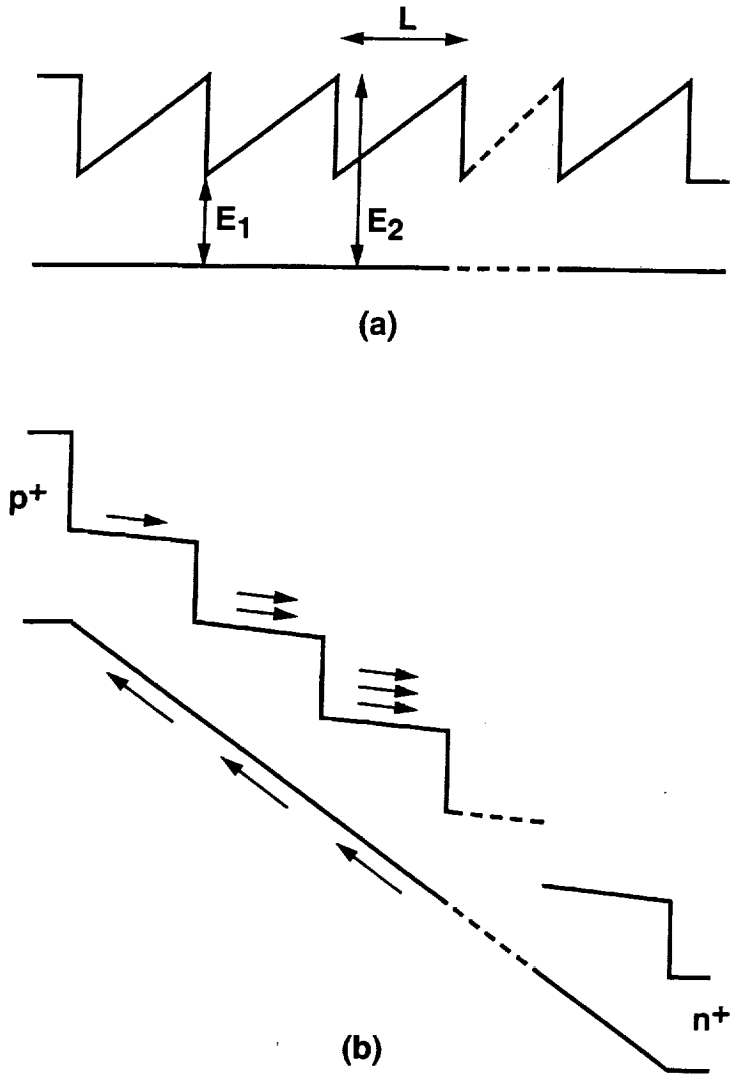

Fig. 16 Energy band diagram of a staircase avalanche photodetector under un-biased and biased conditions. Valence band steps are assumed negligible, and so holes do not impact ionize and only electrons multiply. (a) Unbiased condition, and (b) Biased condition.